Parvalbumin basket cell myelination accumulates axonal mitochondria to internodes

Koen Kole[1]*, Bas J. B. Voesenek[1], Maria E. Brinia[1,3], Naomi Petersen[1] & Maarten H. P. Kole[1,2]*

* Corresponding authors emails: k.kole@nin.knaw.nl and m.kole@nin.knaw.nl

Affiliations

[1] Axonal Signaling Group, Netherlands Institute for Neuroscience, Royal Netherlands Academy of Arts and Sciences, Meibergdreef 47, 1105 BA, Amsterdam, the Netherlands

[2] Cell Biology, Neurobiology and Biophysics, Department of Biology, Faculty of Science, Utrecht University, Padualaan 8, 3584 CH, Utrecht, the Netherlands

[3] Medical School, National Kapodistrian University of Athens, Athens 11527, Greece

Abstract

Parvalbumin-expressing (PV^+) basket cells are fast-spiking interneurons that exert critical control over local neuronal circuit activity and oscillations. PV^+ interneuron axons are partially myelinated but the electrical and metabolic roles of myelin in axonal functions remain poorly understood. Here, we developed Cre-dependent AAV vectors for cell type-specific investigation of mitochondria with genetically encoded fluorescent probes. Single-cell reconstructions and mining of ultrastructural data revealed that mitochondria selectively cluster to myelinated segments of PV^+ basket cell axons. Cuprizone-induced demyelination abolished mitochondrial clustering in PV^+ axons but increased axonal mitochondrial densities in excitatory axons. The internodal clustering of mitochondria was preserved with genetic deletion of myelin basic protein, suggesting that noncompacted myelin is sufficient. Finally, two-photon imaging of action potential-evoked mitochondrial calcium (mt-Ca^{2+}) responses showed that internodal mitochondria did not contribute in buffering activity-dependent Ca^{2+} influx. These findings suggest that oligodendrocyte-PV^+ axon signaling assembles mitochondria to branch selectively fine-tune metabolic demands.

Introduction

In the vertebrate central nervous system, oligodendrocytes wrap multilamellar membranes around axons to form myelin sheaths, which reduce local internodal depolarization, speed up action potential propagation and enhance action potential fidelity[1,2]. Although the myelin sheath strongly facilitates the electrical conductivity of internodes, the insulation also prevents the axolemma from taking up glucose and other metabolites from the extracellular space. Glycolytic oligodendrocytes aid neurons in overcoming this hurdle by providing trophic support to the axon via the myelin sheath in the form of pyruvate and lactate[3,4], and by modulating the function of axonal mitochondria via exosomes[5]. Mitochondria are versatile organelles that are chiefly committed to the production of adenosine triphosphate (ATP), and in axons require metabolic support from the myelin sheath in order to preserve their integrity[6]. Previous research, mostly performed in white matter tracts and glutamatergic axons, has shown that demyelination causes dysfunction and shape changes of axonal mitochondria in both multiple sclerosis (MS)[7–9] and experimental models[10–15]. For example, the mitochondrial size and density increase together with

52 electron transport chain protein expression, and mitochondria lose their membrane potential which
53 is critical for ATP synthesis[7,8,11,14]. The accumulation of mitochondria upon demyelination,
54 together with a low mitochondrial content in myelinated axon and vice versa[16–19], have given rise
55 to the general notion that myelination reduces the need for mitochondria.

56 Myelin is also present around inhibitory GABAergic axons, and in the neocortex nearly
57 exclusively those belonging to parvalbumin-expressing (PV^+) basket cells[20–22]. Comprising the
58 most abundant interneuron cell type in the cortex, PV^+ basket cells are characterized by a highly
59 complex and extensive axonal organization enabling critical control of the local circuitry and over
60 gamma oscillations[23,24]. These interneurons possess small diameter axons (~0.4 µm, ref[25]) which
61 could make them highly vulnerable to pathology of the myelin sheath[26,27]. We recently found that
62 experimental demyelination through toxic or genetic means critically disrupts inhibitory
63 transmission by PV^+ interneurons, characterized by fewer presynaptic terminals, reduced intrinsic
64 excitability and an abolishment of gamma oscillations[22,28]. Interestingly, postmortem studies show
65 that MS is associated with a specific loss in PV^+ interneurons and their presynaptic terminals[28–30].
66 With a low threshold of action potential generation, sustained high firing frequencies and
67 synchronization with fast gamma oscillations, PV^+ interneurons use large amounts of energy to
68 fuel the sodium/potassium ATPase activity to maintain the balance of ionic gradients[31,32]. In line
69 with their high energy usage, PV^+ interneurons are characterized by a relatively high mitochondrial
70 content and cytochrome c oxidase[33,34] while deficits in the spatial distribution of mitochondria in
71 PV^+ axons are associated with impairments of gamma oscillations[35]. One leading hypothesis is
72 that myelination provides trophic support to mitochondria in PV^+ axons to maintain their levels of
73 high-frequency spike generation and activity during gamma oscillations [21,36,37].

74 To examine how myelination affects mitochondrial distribution and function we developed
75 a Cre-dependent viral approach to express mitochondria-targeted genetically encoded fluorescent
76 reporters, mt-GFP and mt-GCamp6f in Cre-driver lines. Two-photon guided patch-clamp
77 recordings from PV^+ interneurons of the somatosensory cortex followed by confocal microscopy
78 and reconstructions with submicron precision revealed that in normally myelinated axons
79 mitochondria are clustered to myelinated segments of PV^+ axons, which was disrupted following
80 experimental demyelination. Analyses of a publicly available electron microscopy (EM) data set[38]
81 confirmed the higher mitochondrial content in myelinated segments of (PV^+) basket cells but
82 showed homogeneous distribution along partially myelinated layer 2/3 pyramidal neurons. In

83 addition, two-photon imaging of action potential-evoked mitochondrial Ca^{2+} transients (mt-
84 GCamp6f) showed that mitochondria in myelinated internodes displayed low or no Ca^{2+} buffering
85 activity, which increased following demyelination. These results indicate that in neocortical PV^+
86 basket cells axons myelination spatially organizes mitochondria, locally increasing the
87 mitochondrial content within internodes, revealing a novel and direct metabolic support by
88 myelination.
89
90
91 **Results**
92 *An AAV-mediated approach for cell type-specific labeling of mitochondria*
93 We first developed a Cre-dependent adeno-associated viral (AAV) vector (AAV-EF1a-mt-
94 GFP-DIO; **Figure 1A**) and examined the *in vivo* labelling of mitochondria. The use of an AAV
95 vector allows control over transduction rates to enable single-cell analyses, an important advantage
96 over brain-wide cell type-specific expression[39]. Upon injection into the somatosensory cortex (S1)
97 of either PV-Cre (labelling PV^+ interneurons) or Rbp4-Cre (labelling cortical layer 5 pyramidal
98 neurons) transgenic mice (**Figure 1B**), this viral vector resulted in GFP-labeled mitochondria in
99 molecularly defined cell types (**Figure 1C-F**). Expression of mt-GFP-DIO in PV-Cre; Ai14 mice
100 (expressing tdTomato in PV^+ interneurons) labelled interneurons across cortical layers 2 to 6 at
101 high specificity (243/248 cells or 97.94% mt-GFP^+ cells were $tdTomato^+$; **Figure 1C**; ref[40]).
102 Furthermore, two-photon-guided targeted whole-cell recordings from mt-GFP-expressing (mt-
103 GFP^+) cells revealed that all cells fired action potentials at high frequency (123.41 ± 13.13 Hz
104 upon 500 pA current injection; n = 8 cells from 5 mice). Action potentials were brief in half-width
105 (295.74 ± 2.52 µs; n = 5 cells from 4 mice) and showed a prominent afterhyperpolarization (−15.83
106 ± 2.25 mV; n = 5 cells from 4 mice, **Figure 1D**), consistent with previously described properties
107 of neocortical PV^+ interneurons[32].
108 To examine the Cre dependency of the mt-GFP-DIO AAV vector, we expressed mt-GFP^+
109 in Rbp4-Cre mice, a Cre-driver line commonly used to label cortical layer (L)5 pyramidal neurons
110 (PNs)[41]. In Rbp4-Cre mice, mt-GFP^+ somata were pyramidally shaped, restricted to L5 and
111 possessed a large apical dendrite characteristic of L5 PNs (**Figure 1E**; ref.[42]). Mt-GFP^+ cells in
112 Rbp4-Cre mice always discharged action potentials in low-frequency trains (40.45 ± 4.76 Hz upon
113 500 pA current injection; n = 13 cells from 4 mice) and of comparatively large half width (680.85
114 ± 15.80 µs; n = 11 cells from 4 mice), consistent with the known electrophysiological properties

115 of L5 PN (**Figure 1D, F**; ref.[43]). Mitochondria are motile organelles but are substantially more
116 stationary in adult mice and *in vivo*[44]. We quantified mitochondrial motility in a subset of our mt-
117 GFP$^+$ acutely prepared slices and found that the vast majority (~99%) of mitochondria were stable
118 in both cell types (**Supplementary Figure 1**). Together, these findings indicate that mt-GFP-DIO
119 enables the study of mitochondria in a highly cell-type specific manner.
120

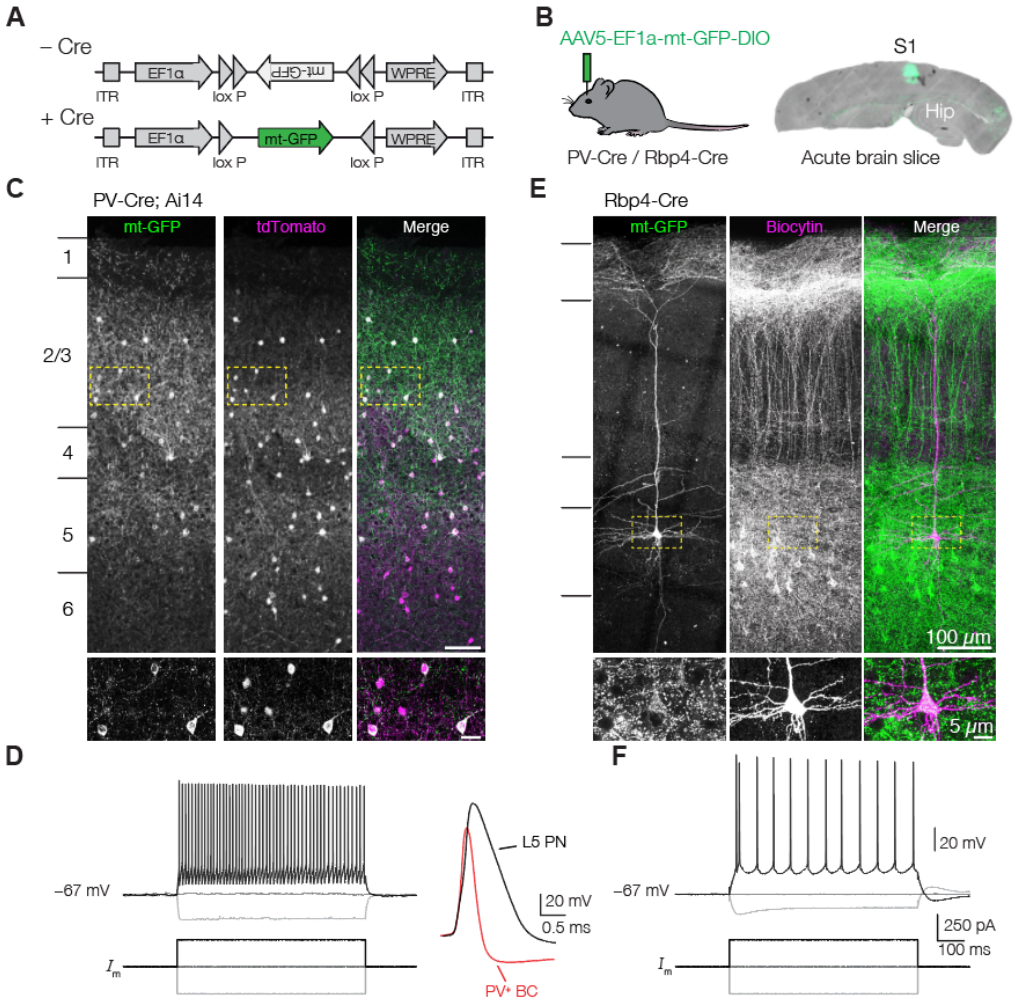

Figure 1 – mt-GFP expresses in a Cre-dependent manner. (A) Schematic of the AAV construct design. Mitochondria-targeted green fluorescent protein (mt-GFP) requires Cre recombination for expression under the EF1α promoter. **(B)** PV-Cre; Ai14 or Rbp4-Cre mice were injected with AAV5-EF1a-mt-GFP-DIO. Hip, hippocampus. **(C)** Expression in PV-Cre; Ai14 mice results in high overlap between tdTomato and mt-GFP. Dashed boxes indicate area depicted by insets at bottom. **(D)** *Left:* Example traces of action potentials in a mt-GFP$^+$ fast spiking PV$^+$ basket cell (BC); *Right*: single action potentials in mt-GFP$^+$ cells from a PV-Cre; Ai14 or Rbp4-Cre mouse (aligned at onset). **(E)** AAV expression in Rbp4-Cre mice results in mitochondrial labeling in L5 PNs. Note the characteristic apical dendrites visualized by mt-GFP. Dashed boxes indicate area depicted by insets at bottom. **f** Example traces of a current-clamp recording and action potential train in a mt-GFP$^+$ L5 PN.

135 *Mitochondria are clustered at the axonal initial segment (AIS) and enlarged upon demyelination*

136 To examine the contribution of myelination to mitochondrial distribution we injected PV-
137 Cre; Ai4 mice with AAV-EF1a-mt-GFP-DIO in S1 and fed mice either with control food or a diet
138 supplemented with 0.2% cuprizone, which selectively kills oligodendrocytes, leading to
139 widespread cortical demyelination[45]. We first focused on the axon initial segment (AIS), a highly
140 excitable domain at the base of the axon where action potentials (APs) are initiated and which is
141 known to adapt to demyelination[43,46]. The AIS was identified by immunostaining for the anchoring
142 protein βIV spectrin in cortical tissue from mt-GFP-expressing PV-Cre; Ai14 mice. By contouring
143 of the perimeter of mt-GFP signals we subsequently estimated the shape and size of mitochondria.
144 The results showed that the mitochondrial area was significantly increased in axons from
145 cuprizone-treated mice (nested t-test, $P = 0.0241$; **Figure 2A-C**). In contrast, the mitochondrial
146 aspect ratio (length/width) and density were unaffected (**Figure 2D-E**).

147 Both the AIS length and distance relative to the soma were comparable between groups
148 (**Figure 2F-G**). AIS length and location are critical to the current threshold for AP generation[47].
149 To test whether AP initiation was preserved we performed whole-cell recordings from PV^+
150 interneurons in acute slices. In all slice experiments, we recorded features of excitability in
151 artificial cerebral spinal fluid containing 5 mM L-lactate and 10 mM D-glucose, resembling the *in*
152 *vivo* extracellular environment containing lactate and low amounts of glucose[48]. In accordance
153 with the unaffected geometrical properties of the AIS, electrophysiological recordings of PV^+
154 interneurons revealed no change in AP wave form, voltage or current threshold, amplitude, half-
155 width, or resting membrane potential (**Figure 2H-I**; **Supplementary Figure 2**). However,
156 demyelinated PV^+ interneurons displayed a higher rheobase (**Figure 2J**), a lower input resistance
157 (**Figure 2K**), and lower firing rate upon sustained somatic current injection (**Figure 2L-M**)
158 indicating reduced excitability, in line with previous recordings[22]. Together, these results show
159 that following demyelination PV^+ interneuron excitability is reduced, and AIS mitochondria are
160 larger.

161

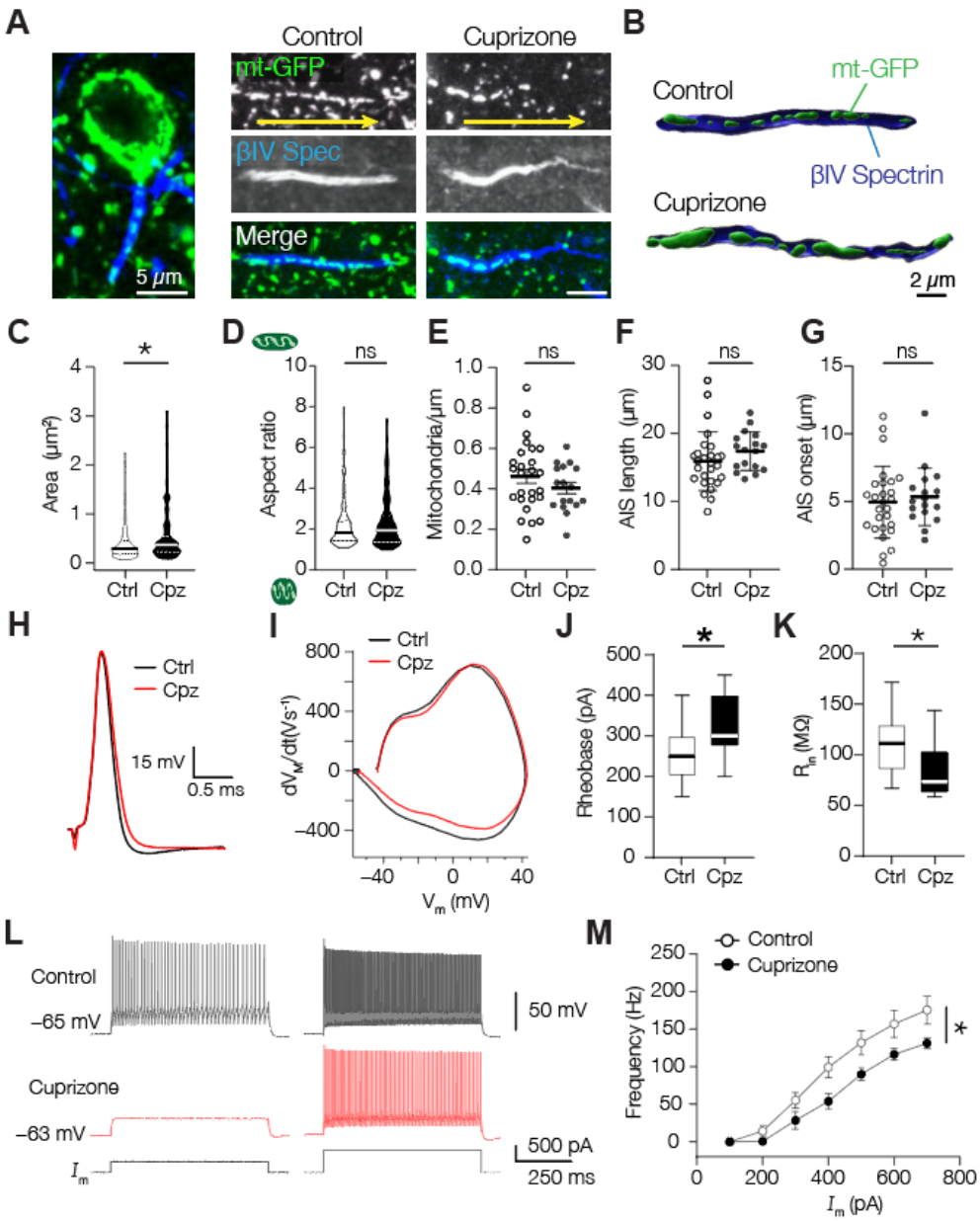

Figure 2 – Cuprizone-induced demyelination enlarges AIS mitochondria and reduces PV$^+$ interneuron excitability (A) Example images of mitochondria (green) at the AIS (blue) of PV$^+$ interneurons. Arrows (yellow) indicate anterograde direction of the axon. **(B)** 3D surface rendering of PV$^+$ AISs containing mitochondria of control or cuprizone-treated axons. **(C)** Mitochondrial area is increased upon demyelination (nested t-test, *P = 0.0241; df = 43; Ctrl, n = 215 mitochondria in 27 AISs from 4 mice; Cpz, n = 144 mitochondria in 18 AISs from 3 mice). **(D)** Mitochondrial aspect ratio is unaffected (nested t-test, P = 0.5656; df = 43; Ctrl, n = 215 mitochondria in 27 AISs from 4 mice; Cpz, n = 144 mitochondria in 18 AISs from 3 mice). **(E)** Density of AIS mitochondria is unchanged upon demyelination (unpaired t-test, P = 0.2396; df = 41; Ctrl, n = 27 AISs from 4 mice; Cpz, n = 17 AISs from 3 mice). **(F)** AIS length is unaffected by cuprizone-treatment (unpaired t-test, P = 0.2112; df = 0.42; Ctrl, n = 27 AISs from 4 mice; Cpz, n = 17 AISs from 3 mice). **(G)** AIS distance (soma edge to AIS) is comparable between control and cuprizone-treated

175 groups (unpaired t-test, $P = 0.6055$; df = 42; Ctrl, $n = 27$ AISs from 4 mice; Cpz, $n = 17$ AISs from
176 3 mice). **(H)** Example single APs of a control and demyelinated PV^+ interneuron upon a 3 ms
177 current injection. **(I)** Phase-plane plots of the traces shown in d; Reduced PV^+ interneuron
178 excitability suggested by **(J)** increased rheobase (unpaired t-test, $*P = 0.0104$; df = 33; Ctrl, $n =$
179 22 cells from 12 mice; Cpz, $n = 13$ cells from 7 mice) and **(K)** reduced input resistance (unpaired
180 t-test, $*P = 0.0337$; df = 33; Ctrl, $n = 22$ cells from 12 mice; Cpz, $n = 13$ cells from 7 mice). **(L)**
181 Example traces of PV^+ interneuron responses after control (black) or cuprizone (red) treatment in
182 response to 400 (left) or 600 pA (right) current injection. **(M)** Population data showing a reduced
183 firing frequency upon somatic current injection in demyelinated PV^+ interneurons (two-way
184 ANOVA with Bonferroni's post hoc test; interaction effect, $P = 0.0215$, $F_{(6, 126)} = 2.582$; treatment
185 effect $*P = 0.0439$, $F_{(1, 21)} = 4.596$; Ctrl, $n = 17$ cells from 12 mice; Cpz, $n = 11$ cells from 7 mice).
186 In truncated violin plots (c, d), solid lines represent the median, dotted lines represent 25th and 75th
187 quartiles. Scatter plots (e-g) indicate the mean, individual data points represent cells, error bars
188 indicate SEM; Box plots (j, k) represent the 25th to 75th percentiles, whiskers indicate the maximal
189 and minimal values, solid line represents the median.
190
191
192 *Mitochondria of the demyelinated PV^+ axon are increased in size and lost in proximal branches*
193 To examine the mitochondrial morphology and distribution throughout the entire cytoarchitecture
194 we reconstructed mt-GFP^+ axons and dendrites of whole-cell recorded biocytin-filled PV^+
195 interneurons (**Supplementary Figs. 3, 4**). Axonal mitochondria in PV^+ interneurons were often
196 found at branch points and *en passant* boutons and were smaller in appearance compared to their
197 dendritic counterparts (**Supplementary Figure 3**; ref.[49]). Quantification showed that compared to
198 dendritic mitochondria those in axons covered significantly less length, were smaller and more
199 spherical (**Supplementary Figure 3**). These morphological differences between mitochondria are
200 in agreement with previous findings in L2/3 PNs [50] and the observed mitochondrial properties in
201 L5 PNs (**Supplementary Figure 4**).
202 Consistent with our observations at the AIS, demyelination significantly increased the size
203 of axonal mitochondria (**Figure 3A-B**), with a mean surface area increase of ~60% (nested t-test,
204 $P = 0.044$; **Figure 3B-C**), without affecting mitochondrial shape (**Figure 3D**), suggesting a
205 uniform increase. Importantly, PV^+ interneuron myelination is most abundant at lower axonal
206 branch orders ($\leq$ 4th order)[20,21,25]. To test whether demyelination affects axonal mitochondria
207 differently we separated the distal population from the 2nd to 4th branch orders and found that the
208 demyelination-induced mitochondrial size increase was comparable (**Figure 3E**).
209 The PV axons did not show signs of swellings or degradation and, consistent with previous
210 work[22], the total reconstructed axonal length was similar between control and demyelinated axons

211 (unpaired t-test, P = 0.4918; **Figure 3G**). Interestingly however, quantification by branch order
212 revealed an increased average segment length in proximal branches of demyelinated PV^+ axons
213 (**Figure 3H**). The observation of local structural changes, together with previous work showing
214 that demyelination increases mitochondrial density[7,8,12], prompted us to investigate the
215 mitochondrial density in PV^+ axons. While the total mitochondrial density across all branches was
216 comparable between control and demyelinated PV^+ axons (unpaired t-test, $P = 0.1170$; **Figure 3I**),
217 mitochondria in the proximal branch orders of demyelinated axons were on average ~20% reduced
218 in density (two-way ANOVA, branch order × treatment effect, $P = 0.0169$; **Figure 3J**). In higher
219 branch orders (≥ 5) the mitochondrial densities were similar between groups (two-way ANOVA
220 with Bonferroni's post hoc test, $P > 0.9999$). In line with these observations, we found an increased
221 inter-mitochondrial distance specifically in proximal branches of demyelinated axons (≤ 4th order;
222 Kruskal-Wallis test with Dunn's post hoc test, $P < 0.0001$; **Figure 3K**). These results are surprising
223 since previous studies consistently reported mitochondria increase in demyelinated axons[12,13]. To
224 examine mitochondria specifically in glutamatergic L5 axons we used a similar viral strategy in
225 Rbp4-Cre mice and examined mitochondrial density in the white matter below the somatosensory cortex.
226 In contrast to the mitochondria loss in PV^+ interneurons we found a *higher* density of mitochondria
227 after cuprizone-mediated demyelination (unpaired t-test, $P = 0.0441$; **Supplementary Figure 5**).
228 Together, these results indicate that myelin loss results in a reduced mitochondrial clustering
229 specifically in the proximal and putatively demyelinated branches of the PV^+ axon.
230
231

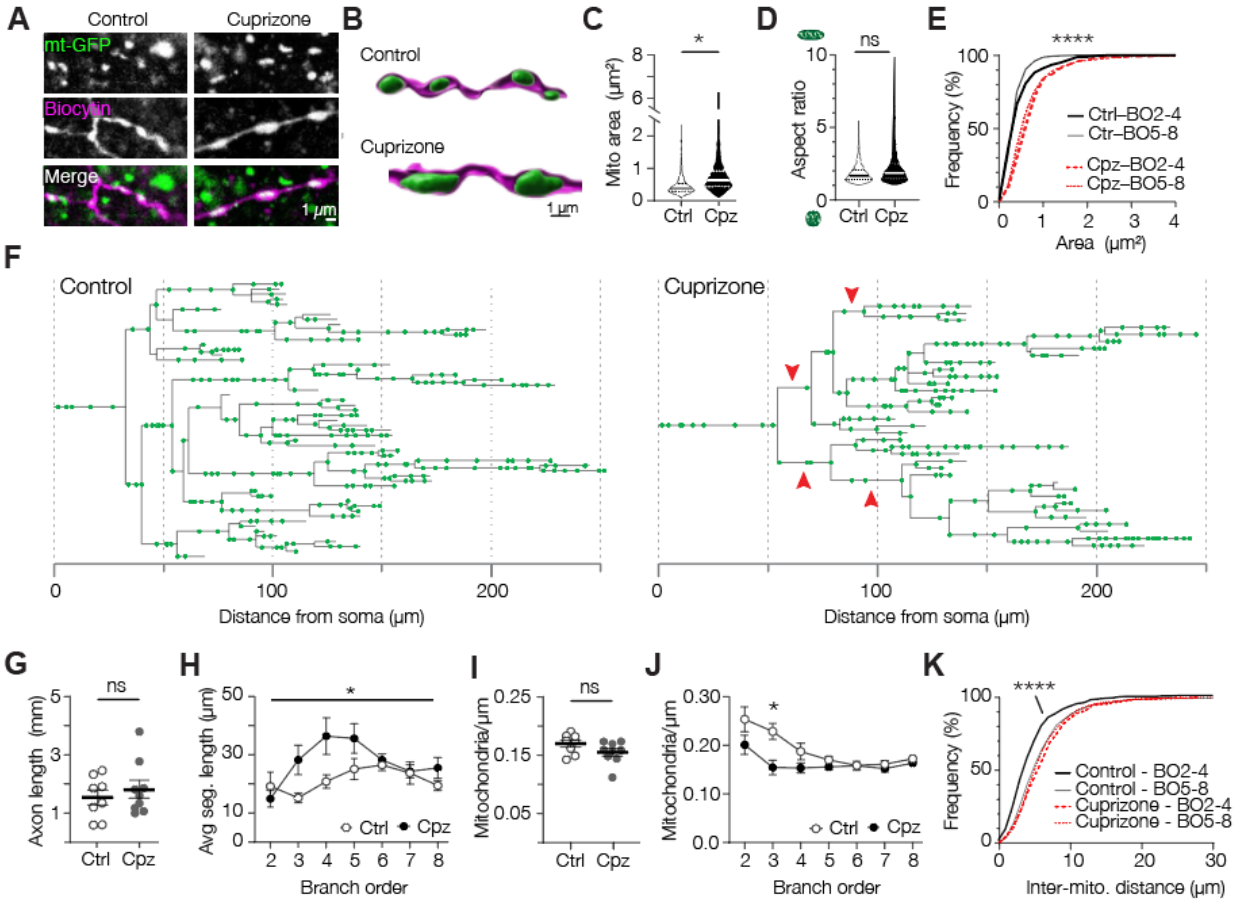

Figure 3 – Cuprizone-induced demyelination reduces mitochondrial density in proximal PV$^+$ interneuron axons. (A) Example confocal images of mitochondria (mt-GFP) in control (left) and demyelinated axon (right). **(B)** 3D rendered images of mt-GFP and biocytin. **(C)** Increased mitochondrial size upon demyelination (nested t-test, *P = 0.038; df = 8; Ctrl, n = 5 axons, 805 mitochondria; 5 cells from 3 mice, Cpz, n = 5 axons, 1218 mitochondria; 5 cells from 4 mice). **(D)** Unchanged mitochondrial aspect ratio in demyelinated axons (nested t-test, P = 0.2962; df = 8; Ctrl, n = 5 axons, 805 mitochondria; 5 cells from 3 mice; Cpz, n = 5 axons, 1218 mitochondria; 5 cells from 4 mice). **(E)** Cumulative distribution plots of mitochondrial size showing uniform increase across all branch orders (BO, Kruskal-Wallis test ****P < 0.0001; Dunn's post hoc test, All Ctrl vs Cpz comparisons, P < 0.0001, Ctrl BO 2-4 vs BO 5-8, P = 0.8402; Cpz BO 2-4 vs BO 5-8, P = 0.3932. Ctrl, n = 5 axons, 805 mitochondria; 5 cells from 3 mice. Cpz, n = 5 axons, 1218 mitochondria; 5 cells from 4 mice). **(F)** Example axonograms of a control- (*left*) and a cuprizone-treated (*right*) PV$^+$ interneuron. Red arrowheads indicate examples of second, third or fourth branch orders where mitochondria appear relatively sparse. **(G)** Cuprizone treatment induces no change in axonal length (unpaired t-test, P = 0.4918; df = 15; Ctrl, n = 8 axons, 5 mice; Cpz, n = 9 axons, 5 mice). **(H)** Increased segment length in demyelinated PV$^+$ axons as a function of branch order (two-way ANOVA; branch order x treatment effect, *P = 0.0440, $F_{(6,90)}$ = 2.266; branch order effect, P = 0.0104, $F_{(3.916, 58.71)}$ = 3.660; treatment effect, P = 0.0479, $F_{(1,15)}$ = 4.639; Bonferroni's post hoc test n.s.; Ctrl, n = 8 axons, 5 mice; Cpz, n = 9 axons, 5 mice). **(I)** No change in overall axonal

253 mitochondrial density (unpaired t-test, $P = 0.1170$; df = 15; Ctrl, $n = 8$ axons, 5 mice; Cpz, $n = 9$
254 axons, 5 mice). **(J)** Reduced mitochondrial density in proximal (< 5) but not distal branch orders
255 (two-way ANOVA, Branch order x treatment effect, $P = 0.0169$, $F_{(6,90)} = 2.747$; branch order effect,
256 $P < 0.0001$, $F_{(2.764, 41.45)} = 9.560$; treatment effect, $P = 0.0143$, $F_{(1,15)} = 7.679$; Bonferroni's post hoc
257 test Branch order 3, $^*P = 0.0340$; Ctrl, $n = 8$ axons, 5 mice; Cpz, $n = 9$ axons, 5 mice). **(K)**
258 Cumulative distribution plot showing increased distance between mitochondria in second to fourth
259 branch orders of demyelinated axons but no change in later branch orders (Kruskal-Wallis test $P <$
260 0.0001; Dunn's post hoc test, Ctrl vs Cpz BO2-4, $^{****}P < 0.0001$; Ctrl BO2-4 vs Ctrl BO5-8, $P <$
261 0.0001; Cpz BO2-4 vs Cpz BO5-8, $P = 0.6008$; Ctrl, $n = 8$ axons, 5 mice; Cpz, $n = 9$ axons, 5
262 mice). Solid lines in truncated violin plots (c, d) represent the median, dotted lines represent 25th
263 and 75th quartiles. Horizontal bars (g, i) represent the mean, individual data points represent axons,
264 error bars represent SEM.
265

266 *Mitochondria are clustered at the myelinated PV$^+$ axon*

267 The loss of mitochondrial clustering in proximal axons following demyelination suggests that
268 mitochondrial distribution is determined, at least in part, by the presence of the myelin sheath. If
269 internode myelination is sufficient to cluster mitochondria this should be visible in the proximal
270 axon arbors of normally myelinated PV$^+$ interneurons, which are characterized by heterogeneous
271 myelin patterns[20,21,25]. To test this, we performed a triple staining for myelin basic protein (MBP),
272 GFP and biocytin in sections from control mice and reconstructed PV$^+$ axons to quantify the
273 mitochondrial density in MBP positive (MBP$^+$) and negative (MBP$^–$) axonal segments (**Figure**
274 **4A-B**, **Supplementary Figure 6**). In agreement with previous findings[20], MBP$^+$ segments were
275 ~19 µm in length (on average 18.59 ± 1.84 µm, range: 2.56–47.62 µm, $n = 32$ internodes).
276 Interestingly, axonal mitochondria in myelinated segments were larger (nested t-test, $P = 0.0121$;
277 **Figure 4C**), and more elongated compared to mitochondria in unmyelinated branches (nested t-
278 test, $P = 0.0388$; **Figure 4D**). We observed that MBP$^+$ segments contained more mitochondria
279 (paired t-test, $P = 0.0013$, **Figure 4E**), and were also significantly longer than MBP$^–$ segments
280 (paired t-test, $P = 0.0267$, **Figure 4F**). Consistent with our hypothesis, after correcting for length,
281 MBP$^+$ axonal segments displayed a significantly higher mitochondrial density compared to MBP$^–$
282 segments of the same axon and comparable branch orders (**Figure 4A-B**, **G**). Furthermore,
283 mitochondrial densities in control MBP$^–$ segments were not different from cuprizone-induced
284 demyelinated PV$^+$ axons (One-way ANOVA, $P = 0.0138$; Bonferroni's post hoc test, MBP$^–$ vs.
285 MBP$^+$ $P = 0.0356$, MBP$^+$ vs. cuprizone BO3 $P = 0.0276$; MBP$^–$ vs cuprizone BO3 $P > 0.9999$).
286 These results support the idea that myelin wrapping alone suffices to cluster and increase the size
287 of mitochondria locally within PV$^+$ internodes.

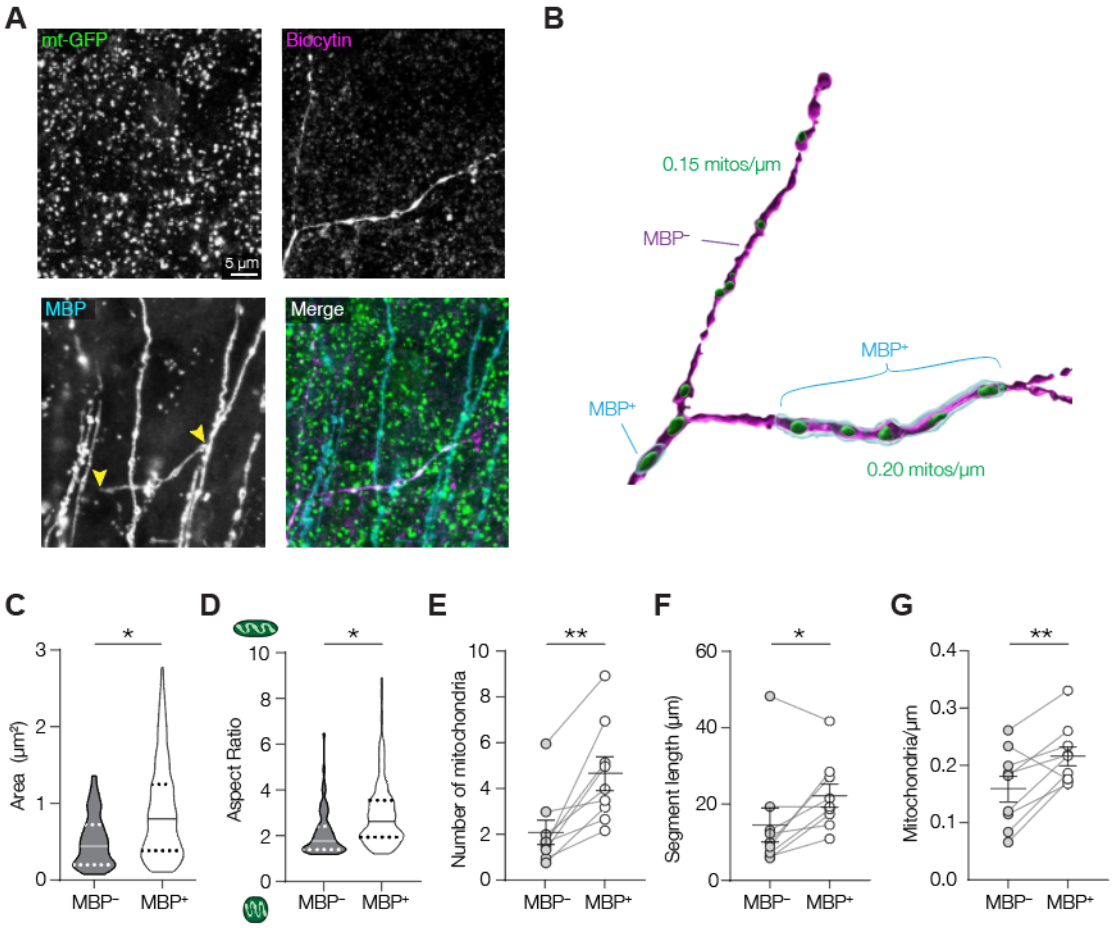

Figure 4 – Mitochondria are clustered to myelinated segments of PV$^+$ axons. (A) Confocal images of a control PV$^+$ axon branch point with one myelinated (MBP$^+$) and one unmyelinated (MBP$^-$) daughter branch. **(B)** 3D surface rendering of the confocal images in a. **(C)** Mitochondrial area is higher at the myelin sheath (nested t-test, P = 0.0121; df = 14; unmyelinated, n = 68 mitochondria; myelinated, n = 114 mitochondria, 8 axons from 6 mice). **(D)** Mitochondrial aspect ratio is significantly higher in myelinated axons (nested t-test, P = 0.0388; df = 14; unmyelinated, n = 68 mitochondria; myelinated, n = 114 mitochondria, 8 axons from 6 mice). **(E)** More mitochondria in MBP$^+$ segments (paired t-test,**P = 0.0013, df = 8; n = 9 axons from 6 mice). **(F)** Myelinated PV$^+$ axonal segments are significantly longer (paired t-test, *P = 0.0267, df = 8; n = 9 axons from 6 mice). **(G)** Mitochondrial density in the myelinated segment is higher compared to unmyelinated ones within the same axon (paired t-test, **P = 0.0099; n = 9 axons from 6 mice). Solid lines in truncated violin plots (c, d) represent the median, dotted lines represent 25th and 75th quartiles, individual data points represent axons (1-4 segments per axon).

307 *Myelination clusters mitochondria selectively to baskets cell internodes*

308 The unexpected axonal mitochondrial clustering within myelinated PV^+ BC internodes
309 could be a common feature of axon-glia signalling along intermittently myelinated axons. To test
310 this, we used a recently published, fully annotated and minable 3D electron microscopy (EM)
311 dataset of the mouse visual cortex[38]. We identified (putative PV^+) basket cells based on their
312 morphological properties and presence of myelinated arbours (**Figure 5A**; see Methods) and
313 compared axonal mitochondrial distribution with those of the primary axons of L2/3 PNs which
314 are known to exhibit patchy distribution of myelin along the primary axon[51] (**Figure 5B**).

315 Consistent with our immunofluorescence analysis, basket cell myelinated segments were
316 significantly longer (two-way ANOVA with Bonferroni's post hoc test, P = 0.0004,
317 **Supplementary Figure 6**). Within basket cell axons mitochondria were found in ~60% of branch
318 points with at least one myelinated branch (presumed nodes; **Supplementary Figure 6**).
319 Interestingly, mitochondria typically avoided ~2 µm regions near the edges of the myelin sheath
320 corresponding to the paranodal loops[17,52], but were with high probability and high densities
321 distributed within the internode (**Supplementary Figure 6**). Myelinated segments of basket cells,
322 both quantitatively and qualitatively in line with the immunoanalysis (Figure 4), had an increased
323 mitochondrial density compared to unmyelinated ones (two-way ANOVA with Bonferroni's post
324 hoc test, P = 0.0130, **Figure 5C**). Interestingly, mitochondrial density in myelinated internodes of
325 L2/3 PNs was not different compared to upstream or downstream segments that were unmyelinated
326 (two-way ANOVA with Bonferroni's post hoc test, P = 0.1665, **Figure 5C**).

327 Furthermore, in basket cells and in keeping with our immunofluorescence data (c.f. Figure
328 4**)**, mitochondria within myelinated segments were significantly larger (P = 0.0087, **Figure 5D**,
329 **Supplementary Figure 6**). Mitochondrial size was, however, not affected in L2/3 PN axonal
330 segments (two-way ANOVA with Bonferroni's post hoc test, P > 0.9999, **Figure5D**). Strikingly,
331 when comparing the mitochondria between the two cell types, those in basket cells were ~7-fold
332 larger (two-way ANOVA with Bonferroni's post hoc test, P = 0.0009, **Figure 5D**). Consistent
333 with previous reports[25] we noticed that unmyelinated segments were typically thinner. A lower
334 cytoplasmic volume could reduce the need for mitochondria and explain the lower mitochondrial
335 density and smaller mitochondrial size. However, plotting the ratio of mitochondrial to axonal
336 volume showed that mitochondria in myelinated basket cell axons occupied a significantly larger
337 volume compared to unmyelinated branches (two-way ANOVA with Bonferroni's post hoc test,

338 $P = 0.0044$, **Figure 5E**). In L2/3 PNs the relative volume of mitochondria was comparable between
339 myelinated and unmyelinated segments (two-way ANOVA with Bonferroni's post hoc test, $P >$
340 0.9999, **Figure 5E**).

341 Taken together, the 3D EM results provide independent support of our AAV
342 immunofluorescence results, revealing with ultrastructural detail that mitochondria selectively
343 cluster to myelinated PV^+ basket cell internodes. Furthermore, they suggest that the clustering of
344 large mitochondria at myelinated axonal segments is not merely a consequence of patchy
345 myelination but may be specific to PV^+ basket cells.

346
347
348 *Compact myelin is not required for mitochondrial clustering to myelinated PV^+ axons*

349 Our data so far suggest that oligodendroglia myelination directly induces mitochondrial clustering
350 at myelinated internodes in PV^+ axons. Axonal mitochondria are supplied with metabolites from
351 glycolytic oligodendrocytes via a system of cytoplasmic channels within myelin and transported
352 across the adaxonal membrane and axolemma[3,4,53]. To test the role of compact and noncompacted
353 myelin we used the *Shiverer* mouse line. These mice harbour a deletion in the *Mbp* gene severely
354 reducing MBP protein levels and resulting in myelin wrapping with only a few noncompacted
355 oligodendroglial membranes[54,55]. We crossed PV-Cre; Ai14 mice with *Shiverer* mice (PV-Cre;
356 Ai14 × Shiverer) and injected wildtype (Mbp^{WT}) and homozygous (Mbp^{Shi}) mice with AAV-EF1a-
357 mt-GFP-DIO to target GFP to mitochondria of normal or dysmyelinated PV^+ interneurons. Patch-
358 clamp recordings from PV^+ interneurons revealed no differences between Mbp^{WT} or Mbp^{Shi} mice
359 for any of the electrophysiological properties (**Supplementary Figure 7**). During whole-cell
360 recordings, cells were filled with biocytin after which we performed a triple staining for biocytin,
361 GFP and myelin oligodendrocyte glycoprotein (MOG) to identify the location of noncompacted
362 myelin lamellae (**Figure 6A-C**; **Supplementary Figure 7**).
363

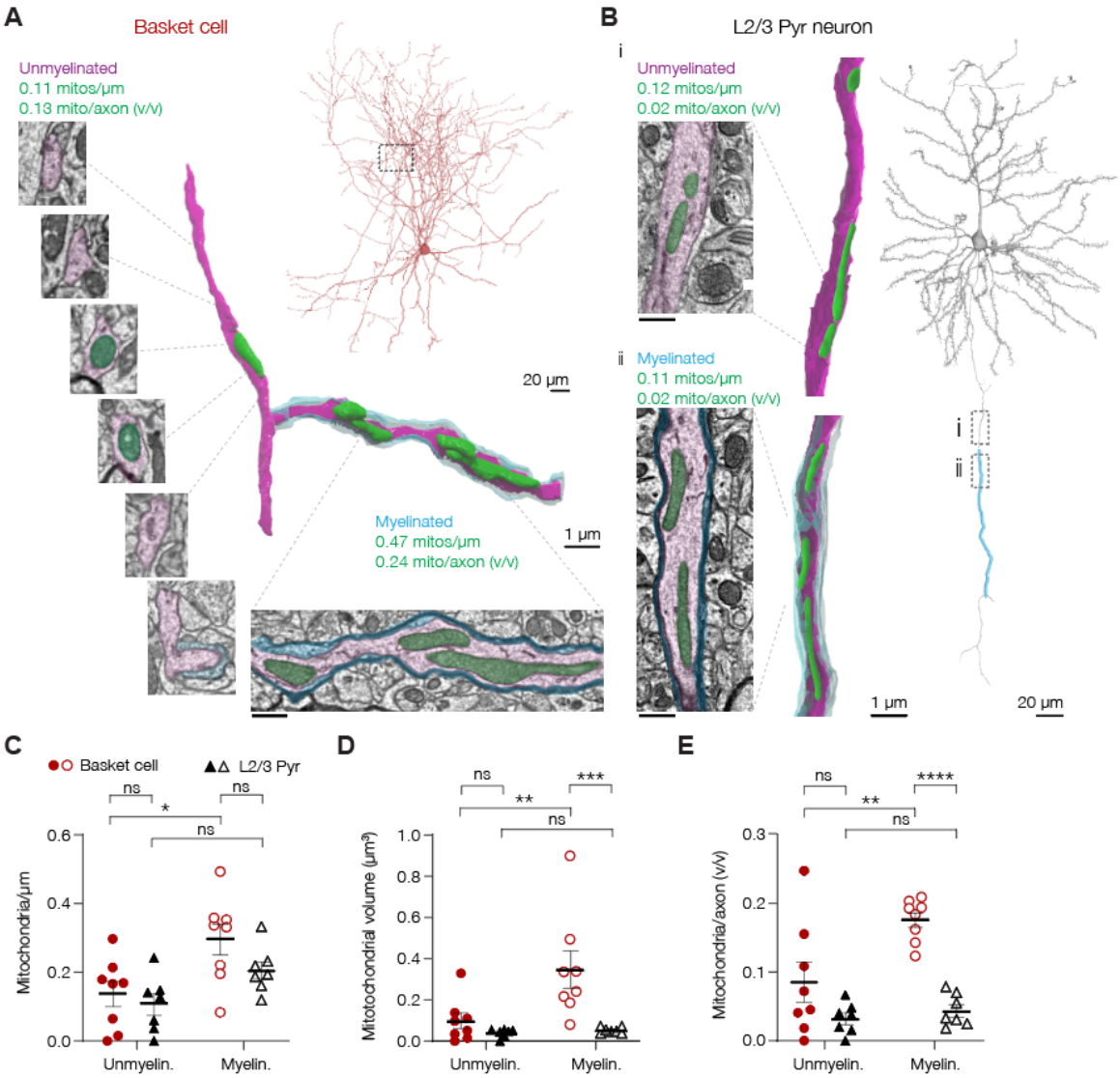

Figure 5 – Myelination assembles mitochondria in basket cell- but not PN internodes. (A-B) 3D EM renders and reconstructions of a basket cell (A) and L2/3 PN (B) axon with and without myelin. **(C)** Mitochondrial density is increased in myelinated basket but not L2/3 PN segments (two-way ANOVA, myelination x cell type effect, $P = 0.4162$, $F_{(1,13)} = 0.7052$; myelination effect, $P = 0.0034$, $F_{(1,13)} = 12.82$; cell type effect, $P = 0.1206$, $F_{(1,13)} = 2.760$; Bonferroni's post hoc test, basket myelin. vs. unmyelin., $*P = 0.0130$; PN myelin. vs. unmyelin., $P = 0.1665$; Myelin. basket vs PN, $P = 0.1766$; Unmyelin. basket vs PN $P > 0.9999$). **(D)** Mitochondria in basket myelinated axonal segments are larger compared to those in PNs (two-way ANOVA, myelination x cell type effect, $P = 0.0430$, $F_{(1,13)} = 5.028$; myelination effect, $P = 0.0285$, $F_{(1,13)} = 6.070$; cell type effect, $P = 0.0043$, $F_{(1,13)} = 11.89$; Bonferroni's post hoc test, basket myelin. vs. unmyelin., $**P = 0.0087$; PN myelinated vs. unmyelin., $P > 0.9999$; Myelin. basket vs PN, $***P = 0.0009$; Unmyelin. basket vs PN $P = 0.9090$; basket, myelin. $n = 68$, unmyelin. $n = 18$ mitochondria; PN, myelin. $n = 53$, unmyelinated $n = 21$ mitochondria). **(E)** In myelinated basket but not PN segments mitochondria take up a larger fraction of the axonal volume (two-way ANOVA, myelination x cell type effect, $P = 0.0410$, $F_{(1,13)} = 5.143$; myelination effect, $P = 0.0117$, $F_{(1,13)} = 8.578$; cell type effect, $P = 0.0002$,

380 $F_{(1,13)} = 27.17$; Bonferroni's post hoc test, basket myelin. vs. unmyelin., $^{**}P = 0.0044$; PN myelin.
381 vs. unmyelin., $P > 0.9999$; Myelin. basket vs PN, $^{****}P < 0.0001$; Unmyelin. basket vs PN $P =$
382 0.0837). Scale bars for EM images in a and b represent 0.5 µm. Bars in c-e represent means, data
383 points in c and e represent individual axons (basket, $n = 8$ cells; PN, $n = 7$ cells; 1-4 segments per
384 cell for each cell type), data points in d represent average mitochondrial volume per cell (basket, n
385 $= 8$ cells, $n = 68$ mitochondria in myelinated and 18 mitochondria in unmyelinated segments; PN,
386 $n = 7$ cells; $n = 21$ mitochondria in myelinated and 53 in unmyelinated segments). Solid horizontal
387 bars indicate means, error bars indicate SEM, individual datapoints indicate cells.
388
389
390 Mitochondria distribution in PV^+ interneurons from Mbp^{WT} mice showed a comparable
391 pattern as found in control mice (**Figure 5, Figure 6**). In brief, we found that mitochondria were
392 both larger and longer in MOG^+ segments compared to those in MOG^- segments (**Figure 6D-E**).
393 We also found more mitochondria in myelinated segments (**Figure 6F**), and myelinated axons
394 were significantly longer than their unmyelinated counterparts (**Figure 6G**). Plotting mitochondria
395 per unit length showed that myelinated axons displayed higher mitochondrial densities compared
396 to those lacking myelin (**Figure 6H**).
397 In the Mbp^{Shi} group, mitochondrial morphology was also myelin-dependent with larger and
398 more tubular mitochondria in MOG^+ segments compared to those in MOG^- branches (two-way
399 ANOVA with Bonferroni's post hoc test; area, $P = 0.0001$, aspect ratio, $P = 0.0069$; **Figure 6D-**
400 **E**). In contrast, the number of mitochondria in MOG^- and MOG^+ axonal arbours were comparable
401 (two-way ANOVA with Bonferroni's post hoc test, $P = 0.2549$; **Figure 6F**). Myelinated segments
402 of PV^+ axons were also shorter in Mbp^{Shi} mice (two-way ANOVA with Bonferroni's post hoc test,
403 $P = 0.0315$; **Figure 6G**), and there was no difference in length between MOG^+ and MOG^-
404 segments (two-way ANOVA with Bonferroni's post hoc test, $P > 0.9999$; **Figure 6G**).
405 Interestingly, when correcting for segment length, there was no difference in mitochondrial density
406 between myelinated and unmyelinated axons (two-way ANOVA with Bonferroni's post hoc test,
407 $P = 0.1070$, **Figure 6H**), due to a significantly increased mitochondrial density in the unmyelinated
408 segments (two-way ANOVA with Bonferroni's post hoc test, $P = 0.0168$, **Figure 6H**). These
409 results provide further evidence that mitochondria are heterogeneously distributed along the
410 proximal arborization of PV^+ axons as a function of myelination. In addition, the presence of
411 noncompacted membrane layers suffices for mitochondrial assembly at internodes.
412

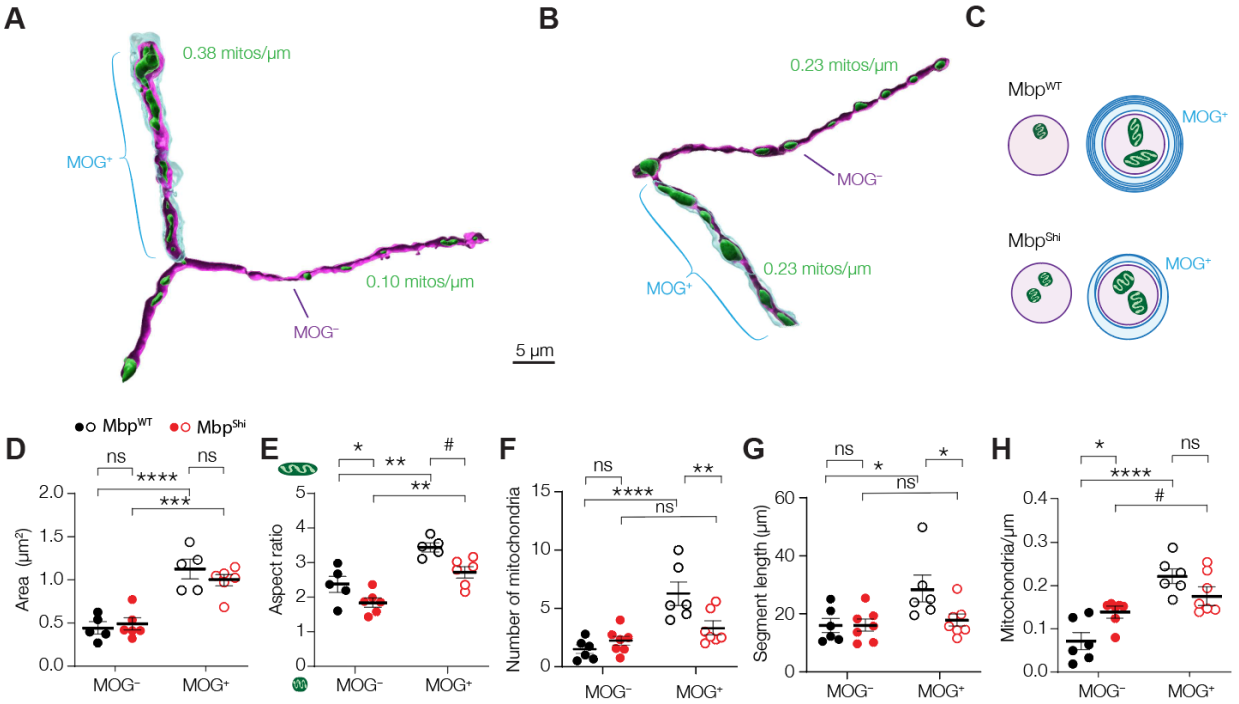

Figure 6 – Noncompacted myelin suffices for internodal mitochondrial clustering. **(A-B)** Example 3D renders of a PV$^+$ axon of a (A) *Mbp*^{WT} or (C) *Mbp*^{Shi} mouse (see Supplementary Figure 7). **(C)** Schematic representation of mitochondrial distributions in *Mbp*^{WT} and *Mbp*^{Shi} PV$^+$ axons. **(D)** Mitochondria under myelin sheaths are larger in both *Mbp*^{WT} and *Mbp*^{Shi} mice (two-way ANOVA, myelination x genotype effect, $P = 0.1481$, $F_{(1, 9)} = 2.504$; myelination effect, $P < 0.0001$, $F_{(1, 9)} = 125.5$; genotype effect, $P = 0.6304$, $F_{(1, 9)} = 0.2480$; Bonferroni's post hoc test, *Mbp*^{WT} MOG$^-$ vs. MOG$^+$, ****$P < 0.0001$; *Mbp*^{Shi} MOG$^-$ vs. MOG$^+$, ***$P < 0.0001$; MOG$^-$ *Mbp*^{WT} vs. *Mbp*^{Shi}, $P > 0.9999$; MOG$^+$ *Mbp*^{WT} vs. *Mbp*^{Shi}, $P = 0.4792$; *Mbp*^{WT}, $n = 6$ cells from 3 mice, MOG$^+$, $n = 72$ mitochondria, MOG$^-$, $n = 28$ mitochondria; *Mbp*^{Shi}, $n = 5$ cells from 3 mice, MOG$^+$, $n = 78$ mitochondria, MOG$^-$, $n = 59$ mitochondria). **(E)** Internode mitochondria in both *Mbp*^{WT} and *Mbp*^{Shi} mice are longer compared to those in unmyelinated axonal segments (two-way ANOVA, myelination x genotype effect, $P = 0.5428$, $F_{(1, 9)} = 0.4000$; myelination effect, $P = 0.0002$, $F_{(1, 9)} = 35.16$; genotype effect, $P = 0.0045$, $F_{(1, 9)} = 14.13$; Bonferroni's post hoc test, *Mbp*^{WT} MOG$^-$ vs. MOG$^+$, **$P = 0.0032$; *Mbp*^{Shi} MOG$^-$ vs. MOG$^+$, **$P = 0.0069$; MOG$^-$ *Mbp*^{WT} vs. *Mbp*^{Shi}, #$P = 0.0825$; MOG$^+$ *Mbp*^{WT} vs. *Mbp*^{Shi}, *$P = 0.0125$; *Mbp*^{WT}, $n = 6$ cells from 3 mice, MOG$^+$, $n = 72$ mitochondria, MOG$^-$, $n = 28$ mitochondria; *Mbp*^{Shi}, $n = 5$ cells from 3 mice, MOG$^+$, $n = 78$ mitochondria, MOG$^-$, $n = 59$ mitochondria). **(F)** Number of mitochondria in PV$^+$ axons of *Mbp*^{WT} and *Mbp*^{Shi} mice (two-way ANOVA, myelination x genotype effect, $P = 0.0027$, $F_{(1, 11)} = 14.77$; myelination effect, $P < 0.0001$, $F_{(1, 11)} = 37.00$; genotype effect, $P = 0.1406$, $F_{(1, 11)} = 2.522$; Bonferroni's post hoc test, *Mbp*^{WT} MOG$^-$ vs. MOG$^+$, ****$P < 0.0001$; *Mbp*^{Shi} MOG$^-$ vs. MOG$^+$, $P = 0.2549$; MOG$^-$ *Mbp*^{WT} vs. *Mbp*^{Shi}, $P = 0.7802$; MOG$^+$ *Mbp*^{WT} vs. *Mbp*^{Shi}, **$P = 0.0041$; *Mbp*^{WT}, $n = 6$ cells from 3 mice; *Mbp*^{Shi}, $n = 5$ cells from 3 mice). **(G)** Segment lengths of PV$^+$ interneuron axons in *Mbp*^{WT} or *Mbp*^{Shi} mice (two-way ANOVA, myelination x genotype effect, $P = 0.0486$, $F_{(1, 11)} = 4.914$; myelination effect, $P = 0.0148$, $F_{(1, 11)} = 8.330$; genotype effect, $P = 0.1348$, $F_{(1, 11)} = 2.605$; Bonferroni's post hoc test, *Mbp*^{WT} MOG$^-$ vs. MOG$^+$, *$P = 0.0104$; *Mbp*^{Shi} MOG$^-$ vs. MOG$^+$, $P > 0.9999$; MOG$^-$ *Mbp*^{WT} vs. *Mbp*^{Shi}, $P > 0.9999$;

439 MOG$^+$ *Mbp*^{WT} vs. *Mbp*^{Shi}, *P = 0.0315; *Mbp*^{WT}, n = 6 cells from 3 mice; *Mbp*^{Shi}, n = 5 cells from 3
440 mice). **(H)** Mitochondrial density is higher in internodes in both *Mbp*^{WT} and *Mbp*^{Shi} mice (two-way
441 ANOVA, myelination x genotype effect, P = 0.0034, $F_{(1, 11)}$ = 13.87; myelination effect, P < 0.0001,
442 $F_{(1, 11)}$ = 44.39; genotype effect, P = 0.4762, $F_{(1, 11)}$ = 0.5441; Bonferroni's post hoc test, *Mbp*^{WT} MOG$^-$
443 vs. MOG$^+$, ****P < 0.0001; *Mbp*^{Shi} MOG$^-$ vs. MOG$^+$, P = 0.1070; MOG$^-$ *Mbp*^{WT} vs. *Mbp*^{Shi}, *P =
444 0.0168; MOG$^+$ *Mbp*^{WT} vs. *Mbp*^{Shi}, P = 0.1919; *Mbp*^{WT}, n = 6 cells from 3 mice; *Mbp*^{Shi}, n = 5 cells from
445 3 mice). Solid horizontal bars indicate means, error bars indicate SEM, individual datapoints indicate
446 cells.
447
448
449
450 *Myelination attenuates mitochondrial Ca^{2+} buffering*
451 The clustering of mitochondria to internodes may be important for the buffering of Ca^{2+}
452 during neuronal activity[50]. Our recent work showed that myelin strongly attenuates but not
453 completely abolishes depolarization of the axolemma enabling activation of internode voltage-
454 gated channels in particular near the node of Ranvier[1]. Indeed, action potential generation has been
455 shown to cause internodal Ca^{2+} influx spreading far from the node of Ranvier[56,57] but to which
456 extent this holds true for PV$^+$ axons and how mitochondria within and outside internodes respond
457 to activity-dependent Ca^{2+} influx is unknown.
458 To examine mitochondrial buffering of Ca^{2+} in we employed AAV-mediated and Cre-
459 dependent expression of the mitochondrion-targeted, genetically encoded calcium indicator mt-
460 GCaMP6f in PV$^+$ interneurons (**Figure 7**). In acute slices of PV-Cre; Ai14 mice we targeted mt-
461 GCaMP6f$^+$ PV$^+$ interneurons for whole-cell patch-clamp recordings and filled them with Atto594,
462 visualizing the arborization of axons during 2P recordings and enabling targeted mitochondrial
463 imaging (**Figure 7A**). In the experiments we imaged mt-Ca^{2+} fluorescence responses following a
464 train of ~100 APs (~143 Hz). In line with previous findings, we observed that during AP trains
465 mitochondria in putative *en passant* boutons of the distal PV$^+$ axon showed strong Ca^{2+} responses,
466 which were unaffected upon demyelination (**Supplementary Figure 8**; ref[50,58]). Similarly, the
467 large amplitude of mt-Ca^{2+} transients at the AIS of PV$^+$ interneurons, was unchanged after
468 demyelination (**Supplementary Figure 8**). These findings suggest that activity-dependent mt-
469 Ca^{2+} buffering in presynaptic terminals and the AIS of PV$^+$ interneurons is preserved after
470 demyelination.
471

472 To test whether there are differences in internodes, unmyelinated and/or demyelinated branches
473 we imaged mt-GCaMP6f along the proximal arbors ($\leq 5^{th}$ branch order) and post-hoc
474 immunostained the slices for GFP, MBP and biocytin, allowing unequivocal assessment of the
475 location of mitochondria with respect to myelin sheaths (**Figure 7B-D**). We first focused on
476 segments (*i.e.* excluding branch points) and found that mitochondria in control axons showed AP-
477 evoked Ca^{2+} responses with greater amplitudes within MBP^{-} segments compared to those in
478 internodes (Kruskal-Wallis test with Dunn's post hoc test, $P < 0.0001$; **Figure 7D**, **Supplementary**
479 **Video 1**). We next asked whether myelin loss would lead to changes in mt-Ca^{2+} buffering in
480 demyelinated PV^{+} interneurons. When we compared all mt-Ca^{2+} responses in control axons
481 (including both MBP^{+} and MBP^{-} segments) with those in putatively demyelinated axons we found
482 no difference between the two groups (nested t-test, $P = 0.6055$). However, mt-Ca^{2+} transients in
483 cuprizone-treated axons were on average larger compared to MBP^{+} control segments (Kruskal-
484 Wallis test with Dunn's post hoc test, $P = 0.0039$; **Figure 7D**) but smaller in amplitude compared
485 to MBP^{-} segments (Kruskal-Wallis test with Dunn's post hoc test, $P = 0.0195$; **Figure 7D**).
486 Mitochondrial Ca^{2+} uptake is known to depend on the influx of extracellular Ca^{2+} (Refs. [58,59]),
487 which in turn is controlled by myelination[56]. To gain a mechanistic insight into how myelination
488 shapes mt-Ca^{2+}, we next examined cytosolic Ca^{2+} (cyt-Ca^{2+}) transients in PV^{+} interneurons. To
489 this end, we expressed GCaMP6f in the cytosol of PV^{+} interneurons and imaged the axonal AP-
490 evoked Ca^{2+} transients in MBP^{+}, MBP^{-} or putatively demyelinated axonal segments. Similar to
491 our results in mitochondria, cyt-Ca^{2+} transient amplitudes were weak in MBP^{+} arbours (Kruskal-
492 Wallis test with Dunn's post hoc test, $P < 0.0001$, **Figure 7F**, **Supplementary Video 2**), while
493 demyelinated axons showed increased Ca^{2+} responses compared to MBP^{+} segments (Kruskal-
494 Wallis test with Dunn's post hoc test, $P = 0.0004$, **Figure 7F**). These results suggest that
495 myelination strongly attenuates internodal Ca^{2+} entry, limiting downstream mt-Ca^{2+} responses in
496 control PV^{+} axons.
497

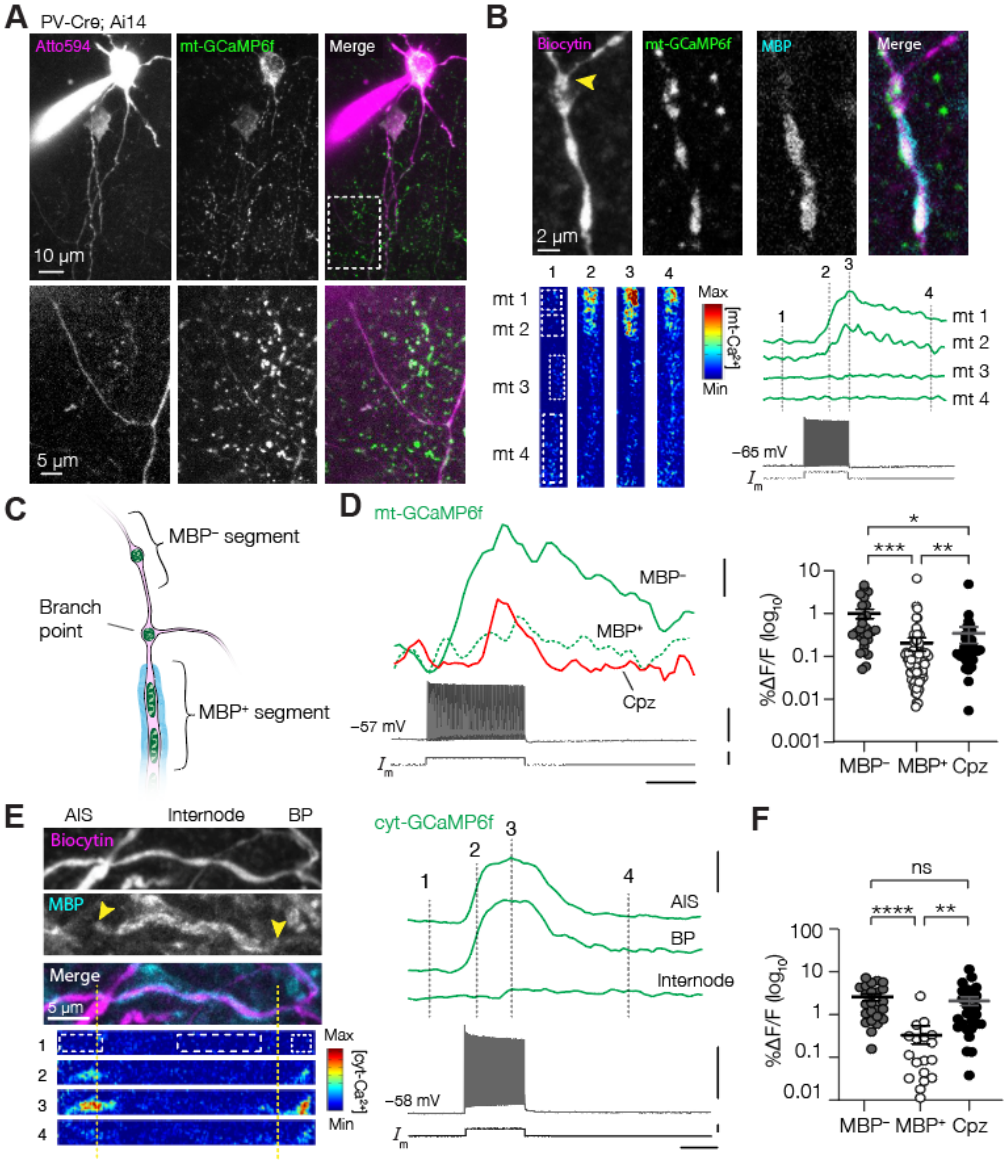

Figure 7. Myelin attenuates internode mt-Ca^{2+} responses. (A) Example 2P image of an Atto594-filled mt-GcaMP6f^{+} PV^{+} interneuron. Dashed box indicates the first branch point of the axon, with a characteristic large angle (≥90°). **(B)** Example control PV^{+} axon with mt-GCaMP6f-labeled mitochondria. Mt-Ca^{2+} responses are stronger in MBP^{-} mitochondria (mito 1 and 2) compared to those in MBP^{+} segment (Mito 3 and 4). Dashed lines indicate timepoints corresponding to the heatmap, yellow arrowhead indicates branch point. Scale bars indicate (top to bottom) 100% ΔF/F, 50 mV, 0.5 nA and 0.5 s. **(C)** Schematic overview of sampled axonal regions. In d, for cuprizone, axonal segments in between branch points were selected. **(D)** *Left*, example Ca^{2+} responses of mitochondria in MBP^{+}, MBP^{-} or putatively demyelinated segments. *Right*, stronger mitochondrial Ca^{2+} responses in MBP^{-} segments compared to MBP^{+} axon and increased Ca^{2+} responses after demyelination (Kruskal-Wallis test, $P < 0.0001$; Dunn's post hoc test MBP^{-} vs., MBP^{+} ***$P < 0.0001$; MBP^{-} vs. cuprizone, *$P = 0.0195$; MBP^{+} vs. cuprizone, **$P = 0.0039$; MBP^{+}, $n = 101$ mitochondria of 12 cells from 7 mice; MBP^{-}, $n = 27$ mitochondria of 10 cells from 6 mice; cuprizone, $n =$

513 36 mitochondria of 10 cells from 5 mice). Scale bars indicate (top to bottom) 25% ΔF/F, 50 mV, 1 nA and
514 0.5 s. **(E)** *Top:* Example confocal image of the AIS, myelinated internode and first branch point of a PV^+
515 axon *Bottom*: time lapse of a two-photon cytosolic (cyt-)GCaMP6f recording of the same axon in response
516 to ~100 APs. Notice only a slight Ca^{2+} response at the MBP edge but practically none in the rest of the
517 internode. Scale bars indicate (top to bottom) 100% ΔF/F, 50 mV, 0.5 nA and 0.5 s. **(F)** Cyt-Ca^{2+} responses
518 are stronger in unmyelinated and demyelinated axonal segments (Kruskal-Wallis test, $P < 0.0001$; Dunn's
519 post hoc test MBP^- vs MBP^+, $P < 0.0001$, MBP^+ vs cuprizone, $P = 0.0004$, MBP^- vs cuprizone, $P = 0.4351$;
520 MBP^+, $n = 18$ segments of 6 cells from 3 mice; MBP^-, $n = 24$ segments of 8 cells from 3 mice; cuprizone,
521 $n = 28$ segments of 6 cells from 3 mice). Solid bars in d and f represent the mean, individual data points in
522 d represent mitochondria, individual data points in f represent segments.
523

524 *Myelin loss impairs mitochondrial Ca^{2+} responses at branch points*

525 Upon closer inspection of the localization of the mitochondria with large mt-Ca^{2+} responses we
526 found that they were in close proximity to the outer edge of the myelin sheath or at branch points
527 (**Figure 7B, 8A**). To further identify the precise localization of the myelin borders we
528 immunostained for Caspr, a paranodal marker, which typically had a length of 2.82 ± 0.18 µm
529 (**Figure 8B**; $n = 36$ $Caspr^+$ segments of 3 cells from 2 mice). The $Caspr^+$ segments often flanked
530 branch points if their branches were myelinated ($n = 19$ branch points of 4 cells from 3 mice,
531 **Figure 8B**). In line with our initial observation, mitochondria were located near $Caspr^+$ signals
532 (range 0.01–16.57 µm, on average 2.46 ± 0.96 µm distance, $n = 20$ paranodes of 4 cells from 3
533 mice; **Figure 8C**). These data suggest that in PV^+ axons branch points are sites of nodes of Ranvier
534 and mitochondria are often found at the nodal domains (**Supplementary Figure 7**).

535 Finally, demyelination is associated with a disassembly of proteins of the node of
536 Ranvier[43,60,61]. In PV^+ axons cuprizone-induced demyelination caused a complete loss of $Caspr^+$
537 segments flanking branch points (0 $Caspr^+$ segments in 4 cells from 3 animals; **Figure 8D**). To
538 investigate how the nodal mt-Ca^{2+} buffering was affected we compared branch point mt-Ca^{2+}
539 transients[42,65]. The results showed that the AP-evoked mt-Ca^{2+} transients in branch points of
540 demyelinated PV^+ axons were lower in amplitude (Mann-Whitney test, $P = 0.0123$; **Figure 8E-**
541 **F**). Moreover, in putatively demyelinated PV^+ axons, mt-Ca^{2+} responses in branch points were
542 indistinguishable from those in unmyelinated axonal segments (Mann-Whitney test, $P = 0.8106$,
543 **Figure 8G**). Similar to the mt-Ca^{2+} responses, we observed that cyt-Ca^{2+} transients at branch points
544 were reduced upon demyelination (Mann-Whitney test, $P = 0.0307$, **Supplementary Figure 8**).
545 Together, these results suggest that cytoplasmic Ca^{2+} influx determines mt-Ca^{2+} buffering, and that

546 the spatiotemporal distribution with hot spots clustered to branch points and low mt-Ca^{2+} responses
547 within the internodes, is disrupted by demyelination (**Figure 9**).
548

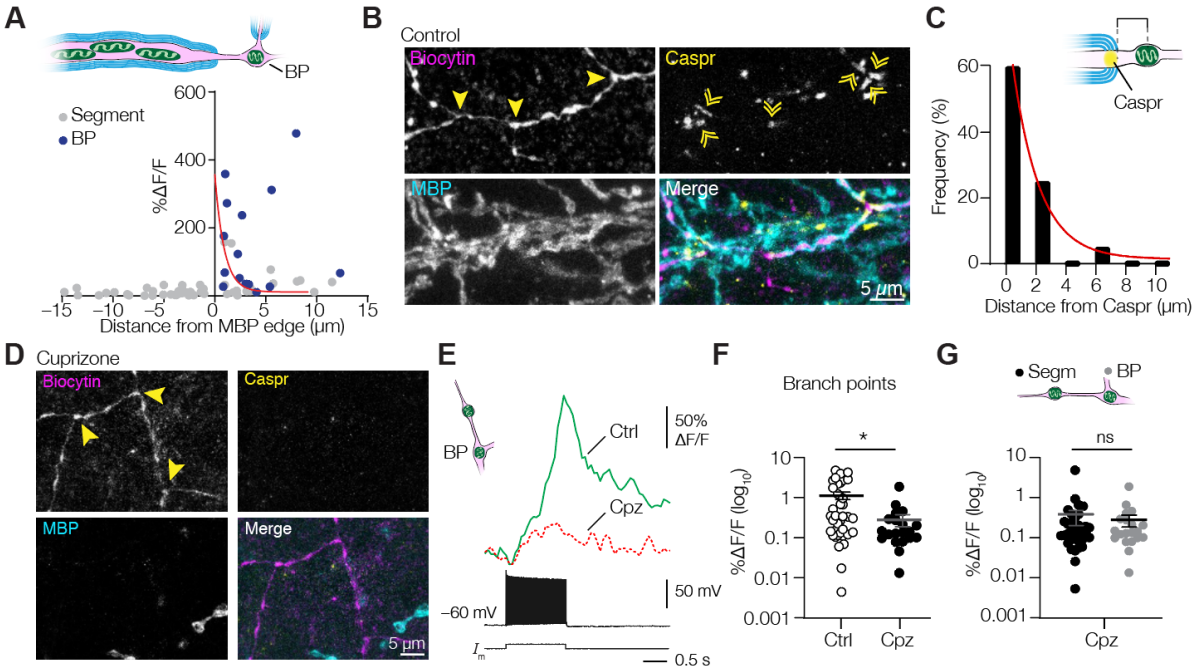

Figure 8 – The mt-Ca^{2+} responses are amplified at nodal domains in PV^{+} axons. (A) Relation between distances from myelin sheaths and mt-Ca^{2+} response amplitude. Red line indicates exponential decay fit (y = (3.588 – 0.1117) × exp(−0.894 × x) + 0.1117); *n* = 62 mitochondria of 9 cells from 6 mice). **(B)** Example confocal images of PV^{+} axon branch points flanked by paranodes (Caspr). **(C)** Mitochondria are frequently found close to paranodes. Red line indicates exponential decay fit (y = (60.73 – 1.415) × exp(−0.5692 × x) + 1.415); *n* = 20 mitochondria of 4 cells from 3 mice. **(D)** Example of PV^{+} axon branch points of a cuprizone-treated mouse. Notice the overall lack of both MBP and Caspr immunostaining. Solid bars in d and e represent the mean, individual data points represent mitochondria. **(E)** *Left:* schematic representation of the compartments investigated in e and f; *Right*: example traces from control or cuprizone-treated axon branch point mitochondria. **(F)** Amplitude of branch point mt-Ca^{2+} responses was reduced upon demyelination (Mann-Whitney test, **P* = 0.0123; control, *n* = 38 mitochondria of 11 cells from 7 mice; cuprizone, *n* = 20 mitochondria of 9 cells from 5 mice). **(G)** In demyelinated PV^{+} axons, mt-Ca^{2+} responses at branch points are indistinguishable from those in segments (Mann-Whitney test, *P* = 0.8106; segment, *n* = 36 mitochondria of 10 cells from 5 mice, same data as Figure 7d; branch points, *n* = 20 mitochondria of 9 cells from 5 mice, same data as in f). BP, branch point. Horizontal bars indicate means, error bars indicate SEM.

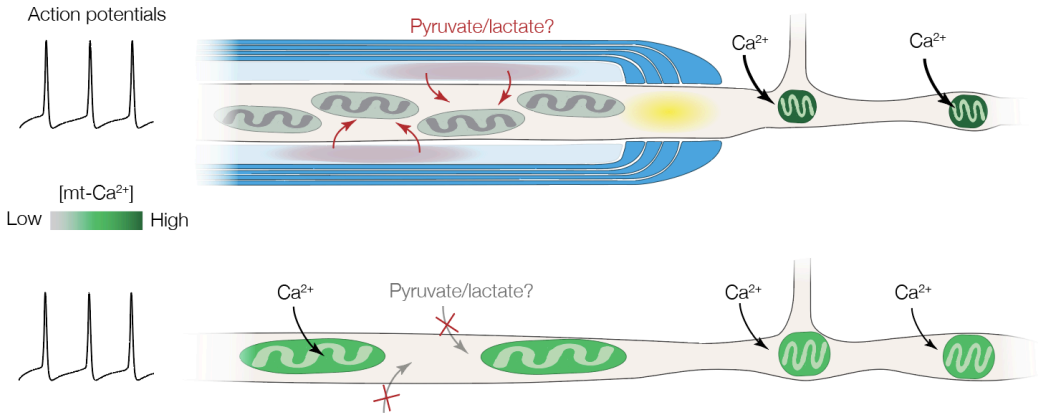

Figure 9 – Summary of the effects of myelin loss on mitochondria in PV$^+$ axons. In normally myelinated PV$^+$ axons (top), mitochondria are clustered at high densities to myelinated internodes (blue), possibly due to local delivery of nutrients such as pyruvate or lactate (red) via cytoplasmic spaces (light blue). Internodal mitochondria avoid the first ~2 µm of the myelin sheath (paranodal domain, yellow), are relatively large, and display no or very weak activity-dependent mt-Ca^{2+} transients (grey). In branch points and unmyelinated segments, mitochondria are smaller but AP-evoked mt-Ca^{2+} transients are large (dark green). Following myelin loss (bottom), mitochondria become larger and sparser at previously myelinated segments, resulting in a more uniform distribution. The mt-Ca^{2+} responses are uniform and low in amplitude (light green) and nodes of Ranvier are lost.

Discussion

We used a Cre recombinase mediated viral approach combined with single-cell reconstructions and found that myelinated segments of PV$^+$ axons have a high mitochondrial content (**Figure 4, 5**). The locally increased number of internodal mitochondria is in striking contrast with the general notion that myelinated axons contain fewer mitochondria[16–19]. In a previous study based on saturated ultrastructural reconstructions of deep layers of the mouse neocortex it was estimated that the mitochondrial content in myelinated axons was a ~30-fold lower compared to unmyelinated axons[19]. However, in that study there was no cell type-specific differentiation. Using a publicly available database[38] we found that the mitochondrial distribution in intermittently myelinated axons differed between (PV$^+$) basket cell interneurons and L2/3 PNs. In contrast to the mitochondrial heterogeneity in interneuron axons, axonal mitochondria are homogeneously distributed across myelinated and unmyelinated segments in excitatory axons. In addition, while demyelination reduced mitochondrial density in PV$^+$ axons it increased

600 mitochondria in excitatory axons in the white matter (**Fig S5**). The latter observation is consistent
601 with a wealth of data indicating that mitochondrial content increases in experimental
602 demyelination and multiple sclerosis[7,10–13].

603 Which factors underlie the cell-type specific clustering of axonal mitochondria in PV^+
604 axons remains to be further examined. One possible explanation is that PV^+ basket cell axons are
605 small in diameter; on average ~0.3 µm for unmyelinated and ~0.6 µm for myelinated segments[25,62].
606 Small diameter axons possess a relatively large membrane surface/cytoplasm ratio limiting axial
607 conductivity for AP propagation but may also require higher energetic costs for axonal
608 transport[63,64] and impede metabolic supply. The energetic demand of the small diameter PV^+
609 interneuron axons is further augmented by the high-frequency firing rates and their generation of
610 gamma frequencies[33]. Taken together, it is tempting to speculate that PV^+ basket cell axon
611 mitochondria efficiently consume the energy supplied by oligodendrocytes. The myelin sheath and
612 axons of GABAergic neurons show multiple distinctive features in their molecular and cellular
613 organization, including the expression of mitochondrial proteins (reviewed in [65]). The hypothesis
614 of a direct external metabolic supply is supported by higher levels of 2',3'-cyclic nucleotide 2'-
615 phosphohydrolase (CNPase)[37]. CNPase is part of the cytoplasmic channels in myelin and the
616 noncompacted inner cytoplasmic loops, involved in lactate and pyruvate supply to the periaxonal
617 space, where these nutrients are shuttled into the axon via monocarboxylate transporters
618 (MCTs)[3,4,6,37]. Indeed, our findings in *Shiverer* mice indicate that noncompacted myelin sufficed
619 to cluster mitochondria at myelin sheaths. Whether oligodendroglial lactate acts as a trophic factor
620 to immobilize axonal mitochondria remains to be tested. Interestingly, high glucose availability
621 has been shown to negatively regulate mitochondrial motility[66]. Furthermore, live imaging in
622 zebrafish axons showed that near paranodes there is myelin-dependent vesicle release[67,68], a
623 process which requires high levels of ATP[69]. ATP consumption by vesicle release, the Na^+/K^+
624 ATPase[70] or axonal transport[71] might cause high local cytoplasmic adenosine diphosphate (ADP)
625 levels, which are known to reduce mitochondrial motility[72] and thereby may potentially cluster
626 mitochondria to PV^+ internodes. Future experiments could image ATP within the internodal
627 domains to test the contribution of internodal mitochondria to local ATP synthesis.

628 To determine the features of motility, Ca^{2+} buffering, anatomical properties of size and
629 shape as well as the distribution of the mitochondria in PV^+ interneurons we used two-photon and
630 confocal microscopy together with 3D EM data, which have been used previously to study

631 mitochondria[7,9,35,50,73]. Confocal imaging has the advantage of allowing the mapping of
632 mitochondria in large parts of single cells from multiple animals but with the tradeoff of a lower
633 spatial resolution. Therefore, we used 3D EM data and could independently verify at the
634 ultrastructural level that mitochondria are larger and more densely distributed at the myelinated
635 PV^+ axon, showing the reliability of our confocal approach. Moreover, the ultrastructural data
636 enabled us to directly investigate mitochondria in different cell types from the same brain. We
637 cannot exclude the possibility that cuprizone affects PV^+ interneuron mitochondria directly, but
638 the increase in mitochondrial size upon demyelination (**Figure 3**) is in keeping with previous
639 studies in axons of other cell types and models of demyelination[7,8,11].

640 Our cyt-Ca^{2+} data shows that the diverse mt-Ca^{2+} responses in PV^+ axons reflect local
641 differentiation of the axon membrane. In normally myelinated axons we observed strong mt-Ca^{2+}
642 influx near branch points which were flanked by $Caspr^+$ signals, suggesting that branch points are
643 sites of nodes of Ranvier, consistent with previous work in GABAergic axons[65,74]. At the nodes
644 APs are regenerated causing large local cytoplasmic Ca^{2+} responses as recorded in other neuron
645 types[56,57,75]. The lower Ca^{2+} transients at these sites in both the cytosol and mitochondria after
646 demyelination might therefore reflect loss of nodal ion channel proteins and/or frequency-
647 dependent failures during our trains of ~100 spikes. These scenarios could be examined in the
648 future using patch-clamp recordings from demyelinated PV^+ axons to achieve a temporal
649 resolution of single APs. Our cyt-Ca^{2+} imaging data indicates that the large mt-Ca^{2+} transients at
650 unmyelinated segments in control axons are caused by large depolarizations that are accompanied
651 by a strong Ca^{2+} influx. It would be informative to use voltage sensitive dye imaging to examine
652 the contribution of axolemmal depolarization[76,77]. Mitochondria in unmyelinated segments may be
653 located near presynaptic GABAergic terminals where voltage-gated Ca^{2+} channels drive major
654 cytoplasmic Ca^{2+} influx[50,58]. However, mt-Ca^{2+} transients near boutons typically show very large
655 amplitudes (**Supplementary Figure 4**) which we did not observe in MBP^- segments.

656 The present finding that myelin clusters mitochondria and defines mitochondrial Ca^{2+}
657 buffering (which also drives ATP synthesis[78]) indicates that myelination patterns may provide an
658 axoglial mechanism to locally regulate energy homeostasis in the PV^+ axon arborization. An
659 important caveat is that with our acute slice preparation the myelination state of the axonal
660 segments prior to demyelination is unknown. Future studies could address this by performing
661 longitudinal *in vivo* imaging. Our AAV approach will be useful to deliver vectors that enable

662 monitoring cytosolic ATP in a cell type-specific manner[79] which will allow the study of axonal
663 ATP levels in (de)myelinated PV^+ interneurons. Our results also have implications for interneuron
664 myelin plasticity[80,81]. Both myelination and proper mitochondrial distribution in PV^+ interneurons
665 are known to be important for gamma oscillations, indicating converging pathways that underly
666 PV^+ interneuron function[22,35]. If in PV^+ interneurons newly formed myelin sheaths attract
667 mitochondria this could represent a novel axoglial mechanism to selectively alter specific axonal
668 paths in the PV^+ axonal trees, subsequently strengthening fast inhibitory transmission of specific
669 neocortical connections. Future research will be necessary to test this hypothesis, by for instance
670 using longitudinal mitochondrial imaging during development of myelination or activity-induced
671 myelination. Finally, the present findings may shed light on the vulnerability of PV^+ basket cells
672 to myelin loss in MS[28–30]. If mitochondria in PV^+ interneuron axons are particularly reliant on the
673 myelin sheath for external metabolic support, myelin loss might acutely and negatively influence
674 axonal transport, ion homeostasis and other critical processes in PV^+ axons. Moreover, the small
675 diameter of basket cell axons could make them more vulnerable to excess Ca^{2+} influx upon
676 demyelination[82], in particular given that mt-Ca^{2+} buffering is insufficient to maintain normal cyt-
677 Ca^{2+} levels during AP trains (**Figure 7**). Together, the data presented here reveal a critical role for
678 myelin to diversify mitochondrial distribution and function in PV^+ axons and encourage future
679 research into mitochondrial dysfunction in PV^+ interneuron axons in MS.
680
681
682
683
684
685

686 **References**

687

688 1. Cohen, C. C. H. *et al.* Saltatory Conduction along Myelinated Axons Involves a Periaxonal
689 Nanocircuit. *Cell* 180, 311-322.e15 (2020).

690 2. Nave, K.-A. & Werner, H. B. Myelination of the Nervous System: Mechanisms and
691 Functions. *Annu Rev Cell Dev Bi* 30, 503–533 (2014).

692 3. Lee, Y. *et al.* Oligodendroglia metabolically support axons and contribute to
693 neurodegeneration. *Nature* 487, 443–448 (2012).

694 4. Fünfschilling, U. *et al.* Glycolytic oligodendrocytes maintain myelin and long-term axonal
695 integrity. *Nature* 485, 517–521 (2012).

696 5. Chamberlain, K. A. *et al.* Oligodendrocytes enhance axonal energy metabolism by
697 deacetylation of mitochondrial proteins through transcellular delivery of SIRT2. *Neuron* (2021)
698 doi:10.1016/j.neuron.2021.08.011.

699 6. Philips, T. *et al.* MCT1 Deletion in Oligodendrocyte Lineage Cells Causes Late-Onset
700 Hypomyelination and Axonal Degeneration. *Cell Reports* 34, 108610 (2021).

701 7. Zambonin, J. L. *et al.* Increased mitochondrial content in remyelinated axons: implications for
702 multiple sclerosis. *Brain* 134, 1901–1913 (2011).

703 8. Witte, M. E. *et al.* Enhanced number and activity of mitochondria in multiple sclerosis lesions.
704 *J Pathology* 219, 193–204 (2009).

705 9. Mahad, D. J. *et al.* Mitochondrial changes within axons in multiple sclerosis. *Brain* 132,
706 1161–1174 (2009).

707 10. Kiryu-Seo, S., Ohno, N., Kidd, G. J., Komuro, H. & Trapp, B. D. Demyelination increases
708 axonal stationary mitochondrial size and the speed of axonal mitochondrial transport. *J Neurosci*
709 30, 6658--66 (2010).

710 11. Nikic, I. *et al.* A reversible form of axon damage in experimental autoimmune
711 encephalomyelitis and multiple sclerosis. *Nat Med* 17, 495--499 (2011).

712 12. Licht-Mayer, S. *et al.* Enhanced axonal response of mitochondria to demyelination offers
713 neuroprotection: implications for multiple sclerosis. *Acta Neuropathol* 140, 143–167 (2020).

714 13. Ohno, N. *et al.* Mitochondrial immobilization mediated by syntaphilin facilitates survival of
715 demyelinated axons. *Proc National Acad Sci* 111, 9953–9958 (2014).

716 14. Licht-Mayer, S. *et al.* Axonal response of mitochondria to demyelination and complex IV
717 activity within demyelinated axons in experimental models of multiple sclerosis. *Neuropath Appl*
718 *Neuro* e12851 (2022) doi:10.1111/nan.12851.

719 15. Andrews, H. *et al.* Increased axonal mitochondrial activity as an adaptation to myelin
720 deficiency in the Shiverer mouse. *J Neurosci Res* 83, 1533–1539 (2006).

721 16. Balaratnasingam, C., Morgan, W. H., Johnstone, V., Cringle, S. J. & Yu, D.-Y.
722 Heterogeneous Distribution of Axonal Cytoskeleton Proteins in the Human Optic Nerve. *Invest*
723 *Ophth Vis Sci* 50, 2824–2838 (2009).

724 17. Perge, J. A., Koch, K., Miller, R., Sterling, P. & Balasubramanian, V. How the Optic Nerve
725 Allocates Space, Energy Capacity, and Information. *J Neurosci* 29, 7917–7928 (2009).

726 18. Kageyama, G. H. & Wong-Riley, M. T. The histochemical localization of cytochrome
727 oxidase in the retina and lateral geniculate nucleus of the ferret, cat, and monkey, with particular
728 reference to retinal mosaics and ON/OFF-center visual channels. *J Neurosci* 4, 2445–59 (1984).

729 19. Kasthuri, N. *et al.* Saturated Reconstruction of a Volume of Neocortex. *Cell* 162, 648–661
730 (2015).

731 20. Stedehouder, J. *et al.* Fast-spiking Parvalbumin Interneurons are Frequently Myelinated in
732 the Cerebral Cortex of Mice and Humans. *Cereb Cortex* 27, 5001–5013 (2017).

733 21. Micheva, K. D. *et al.* A large fraction of neocortical myelin ensheathes axons of local
734 inhibitory neurons. *Elife* 5, e15784 (2016).

735 22. Dubey, M. *et al.* Myelination synchronizes cortical oscillations by consolidating
736 parvalbumin-mediated phasic inhibition. *Elife* 11, (2022).

737 23. Kepecs, A. & Fishell, G. Interneuron cell types are fit to function. *Nature* 505, 318--26
738 (2014).

739 24. Hu, H., Gan, J. & Jonas, P. Fast-spiking, parvalbumin^{+} GABAergic interneurons: From
740 cellular design to microcircuit function. *Science* 345, 1255263 (2014).

741 25. Stedehouder, J. *et al.* Local axonal morphology guides the topography of interneuron
742 myelination in mouse and human neocortex. *Elife* 8, e48615 (2019).

743 26. Edgar, J. M. *et al.* Early ultrastructural defects of axons and axon–glia junctions in mice
744 lacking expression of Cnp1. *Glia* 57, 1815–1824 (2009).

745 27. Evangelou, N. *et al.* Size-selective neuronal changes in the anterior optic pathways suggest a
746 differential susceptibility to injury in multiple sclerosis. *Brain* 124, 1813–1820 (2001).

747 28. Ramaglia, V. *et al.* Complement-associated loss of CA2 inhibitory synapses in the
748 demyelinated hippocampus impairs memory. *Acta Neuropathol* 142, 643–667 (2021).

749 29. Dutta, R. *et al.* Mitochondrial dysfunction as a cause of axonal degeneration in multiple
750 sclerosis patients. *Ann Neurol* 59, 478--489 (2006).

751 30. Zoupi, L. *et al.* Selective vulnerability of inhibitory networks in multiple sclerosis. *Acta*
752 *Neuropathol* 141, 415–429 (2021).

753 31. Hu, H., Roth, F. C., Vandael, D. & Jonas, P. Complementary Tuning of Na+ and K+ Channel
754 Gating Underlies Fast and Energy-Efficient Action Potentials in GABAergic Interneuron Axons.
755 *Neuron* 98, 156-165.e6 (2018).

756 32. Li, T. *et al.* Action Potential Initiation in Neocortical Inhibitory Interneurons. *Plos Biol* 12,
757 e1001944 (2014).

758 33. Kann, O., Papageorgiou, I. E. & Draguhn, A. Highly Energized Inhibitory Interneurons are a
759 Central Element for Information Processing in Cortical Networks. *J Cereb Blood Flow*
760 *Metabolism* 34, 1270–1282 (2014).

761 34. Kageyama, G. H. & Wong-Riley, M. T. T. Histochemical localization of cytochrome oxidase
762 in the hippocampus: Correlation with specific neuronal types and afferent pathways.
763 *Neuroscience* 7, 2337–2361 (1982).

764 35. Kontou, G. *et al.* Miro1-dependent mitochondrial dynamics in parvalbumin Interneurons.
765 *Elife* 10, e65215 (2021).

766 36. Stedehouder, J. & Kushner, S. A. Myelination of parvalbumin interneurons: a parsimonious
767 locus of pathophysiological convergence in schizophrenia. *Mol Psychiatr* 22, 4–12 (2017).

768 37. Micheva, K. D. *et al.* Distinctive Structural and Molecular Features of Myelinated Inhibitory
769 Axons in Human Neocortex. *Eneuro* 5, ENEURO.0297-18.2018 (2018).

770 38. Consortium, Mic. *et al.* Functional connectomics spanning multiple areas of mouse visual
771 cortex. *Biorxiv* 2021.07.28.454025 (2021) doi:10.1101/2021.07.28.454025.

772 39. Fecher, C. *et al.* Cell-type-specific profiling of brain mitochondria reveals functional and
773 molecular diversity. *Nat Neurosci* 22, 1731--1742 (2019).

774 40. Meyer, H. S. *et al.* Inhibitory interneurons in a cortical column form hot zones of inhibition
775 in layers 2 and 5A. *Proc National Acad Sci* 108, 16807--12 (2011).

776 41. Gerfen, C. R., Paletzki, R. & Heintz, N. GENSAT BAC Cre-Recombinase Driver Lines to
777 Study the Functional Organization of Cerebral Cortical and Basal Ganglia Circuits. *Neuron* 80,
778 1368–1383 (2013).

779 42. Hamada, M. S., Goethals, S., Vries, S. I. D., Brette, R. & Kole, M. H. P. Covariation of axon
780 initial segment location and dendritic tree normalizes the somatic action potential. *Proc National*
781 *Acad Sci* 113, 14841--14846 (2016).

782 43. Hamada, M. S. & Kole, M. H. P. Myelin Loss and Axonal Ion Channel Adaptations
783 Associated with Gray Matter Neuronal Hyperexcitability. *J Neurosci* 35, 7272–7286 (2015).

784 44. Smit-Rigter, L. *et al.* Mitochondrial Dynamics in Visual Cortex Are Limited In Vivo and Not
785 Affected by Axonal Structural Plasticity. *Curr Biol* 26, 2609–2616 (2016).

786 45. Kipp, M., Clarner, T., Dang, J., Copray, S. & Beyer, C. The cuprizone animal model: new
787 insights into an old story. *Acta Neuropathol* 118, 723–736 (2009).

788 46. Kole, M. H. P., Letzkus, J. J. & Stuart, G. J. Axon Initial Segment Kv1 Channels Control
789 Axonal Action Potential Waveform and Synaptic Efficacy. *Neuron* 55, 633–647 (2007).

790 47. Kole, M. H. & Brette, R. The electrical significance of axon location diversity. *Curr Opin*
791 *Neurobiol* 51, 52–59 (2018).

792 48. Zilberter, Y., Zilberter, T. & Bregestovski, P. Neuronal activity in vitro and the in vivo
793 reality: the role of energy homeostasis. *Trends Pharmacol Sci* 31, 394–401 (2010).

794 49. Cserep, C., Posfai, B., Schwarcz, A. D. & Denes, A. Mitochondrial ultrastructure is coupled
795 to synaptic performance at axonal release sites. *Eneuro* 5, (2018).

796 50. Lewis, T. L., Kwon, S.-K., Lee, A., Shaw, R. & Polleux, F. MFF-dependent mitochondrial
797 fission regulates presynaptic release and axon branching by limiting axonal mitochondria size.
798 *Nat Commun* 9, 5008 (2018).

799 51. Tomassy, G. S. *et al.* Distinct Profiles of Myelin Distribution Along Single Axons of
800 Pyramidal Neurons in the Neocortex. *Science* 344, 319–324 (2014).

801 52. Edgar, J. M., McCulloch, M. C., Thomson, C. E. & Griffiths, I. R. Distribution of
802 mitochondria along small-diameter myelinated central nervous system axons. *J Neurosci Res* 86,
803 2250–2257 (2008).

804 53. Saab, A. S. & Nave, K.-A. Myelin dynamics: protecting and shaping neuronal functions.
805 *Curr Opin Neurobiol* 47, 104–112 (2017).

806 54. Roach, A., Takahashi, N., Pravtcheva, D., Ruddle, F. & Hood, L. Chromosomal mapping of
807 mouse myelin basic protein gene and structure and transcription of the partially deleted gene in
808 shiverer mutant mice. *Cell* 42, 149–155 (1985).

809 55. Snaidero, N. *et al.* Myelin Membrane Wrapping of CNS Axons by PI(3,4,5)P3-Dependent
810 Polarized Growth at the Inner Tongue. *Cell* 156, 277–290 (2014).

811 56. Hanemaaijer, N. A. *et al.* Ca2+ entry through NaV channels generates submillisecond axonal
812 Ca2+ signaling. *Elife* 9, e54566 (2020).

813 57. Zhang, Z. & David, G. Stimulation-induced Ca2+ influx at nodes of Ranvier in mouse
814 peripheral motor axons. *J Physiology* 594, 39–57 (2016).

815 58. Ashrafi, G., Juan-Sanz, J. de, Farrell, R. J. & Ryan, T. A. Molecular Tuning of the Axonal
816 Mitochondrial Ca2+ Uniporter Ensures Metabolic Flexibility of Neurotransmission. *Neuron* 105,
817 678-687.e5 (2020).

818 59. Stoler, O. *et al.* Frequency- and spike-timing-dependent mitochondrial Ca2+ signaling
819 regulates the metabolic rate and synaptic efficacy in cortical neurons. *Elife* 11, e74606 (2022).

820 60. Crawford, D. K., Mangiardi, M., Xia, X., López-Valdés, H. E. & Tiwari-Woodruff, S. K.
821 Functional recovery of callosal axons following demyelination: a critical window. *Neuroscience*
822 164, 1407–1421 (2009).

823 61. Dupree, J. L. *et al.* Oligodendrocytes assist in the maintenance of sodium channel clusters
824 independent of the myelin sheath. *Neuron Glia Biol* 1, 179–192 (2004).

825 62. Micheva, K. D., Kiraly, M., Perez, M. M. & Madison, D. V. Conduction Velocity Along the
826 Local Axons of Parvalbumin Interneurons Correlates With the Degree of Axonal Myelination.
827 *Cereb Cortex* 31, bhab018- (2021).

828 63. Wortman, J. C. *et al.* Axonal Transport: How High Microtubule Density Can Compensate
829 for Boundary Effects in Small-Caliber Axons. *Biophys J* 106, 813–823 (2014).

830 64. Griffiths, I. *et al.* Axonal Swellings and Degeneration in Mice Lacking the Major Proteolipid
831 of Myelin. *Science* 280, 1610–1613 (1998).

832 65. Mazuir, E., Fricker, D. & Sol-Foulon, N. Neuron–Oligodendrocyte Communication in
833 Myelination of Cortical GABAergic Cells. *Life* 11, 216 (2021).

834 66. Pekkurnaz, G., Trinidad, J. C., Wang, X., Kong, D. & Schwarz, T. L. Glucose Regulates
835 Mitochondrial Motility via Milton Modification by O-GlcNAc Transferase. *Cell* 158, 54–68
836 (2014).

837 67. Mensch, S. *et al.* Synaptic vesicle release regulates myelin sheath number of individual
838 oligodendrocytes in vivo. *Nat Neurosci* 18, 628–630 (2015).

839 68. Almeida, R. G. *et al.* Myelination induces axonal hotspots of synaptic vesicle fusion that
840 promote sheath growth. *Curr Biol* (2021) doi:10.1016/j.cub.2021.06.036.

841 69. Rangaraju, V., Calloway, N. & Ryan, T. A. Activity-Driven Local ATP Synthesis Is
842 Required for Synaptic Function. *Cell* 156, 825–835 (2014).

843 70. Young, E. A. *et al.* Imaging correlates of decreased axonal Na+/K+ ATPase in chronic
844 multiple sclerosis lesions. *Ann Neurol* 63, 428–435 (2008).

845 71. Gennerich, A. & Vale, R. D. Walking the walk: how kinesin and dynein coordinate their
846 steps. *Curr Opin Cell Biol* 21, 59–67 (2009).

847 72. Mironov, S. L. ADP Regulates Movements of Mitochondria in Neurons. *Biophys J* 92, 2944–
848 2952 (2007).

849 73. Turner, N. L. *et al.* Reconstruction of neocortex: Organelles, compartments, cells, circuits,
850 and activity. *Cell* 185, 1082-1100.e24 (2022).

851 74. Benamer, N., Vidal, M., Balia, M. & Angulo, M. C. Myelination of parvalbumin
852 interneurons shapes the function of cortical sensory inhibitory circuits. *Nat Commun* 11, 5151
853 (2020).

854 75. Grundemann, J. & Clark, B. A. Calcium-Activated Potassium Channels at Nodes of Ranvier
855 Secure Axonal Spike Propagation. *Cell Reports* 12, 1715--1722 (2015).

856 76. Popovic, M. A., Foust, A. J., McCormick, D. A. & Zecevic, D. The spatio-temporal
857 characteristics of action potential initiation in layer 5 pyramidal neurons: a voltage imaging
858 study. *J Physiology* 589, 4167–4187 (2011).

859 77. Foust, A. J., Yu, Y., Popovic, M., Zecevic, D. & McCormick, D. A. Somatic Membrane
860 Potential and Kv1 Channels Control Spike Repolarization in Cortical Axon Collaterals and
861 Presynaptic Boutons. *J Neurosci* 31, 15490–15498 (2011).

862 78. Rizzuto, R., Stefani, D. D., Raffaello, A. & Mammucari, C. Mitochondria as sensors and
863 regulators of calcium signalling. *Nat Rev Mol Cell Bio* 13, 566–578 (2012).

864 79. Trevisiol, A. *et al.* Monitoring ATP dynamics in electrically active white matter tracts. *Elife*
865 6, e24241 (2017).

866 80. Stedehouder, J., Brizee, D., Shpak, G. & Kushner, S. A. Activity-Dependent Myelination of
867 Parvalbumin Interneurons Mediated by Axonal Morphological Plasticity. *J Neurosci* 38, 3631–
868 3642 (2018).

869 81. Yang, S. M., Michel, K., Jokhi, V., Nedivi, E. & Arlotta, P. Neuron class–specific responses
870 govern adaptive myelin remodeling in the neocortex. *Science* 370, (2020).

871 82. Persson, A.-K., Hoeijmakers, J. G. J., Estacion, M., Black, J. A. & Waxman, S. G. Sodium
872 Channels, Mitochondria, and Axonal Degeneration in Peripheral Neuropathy. *Trends Mol Med*
873 22, 377–390 (2016).

874 83. Aurnhammer, C. *et al.* Universal Real-Time PCR for the Detection and Quantification of
875 Adeno-Associated Virus Serotype 2-Derived Inverted Terminal Repeat Sequences. *Hum Gene*
876 *Ther Part B Methods* 23, 18–28 (2012).

877 84. Berger, D. R., Seung, H. S. & Lichtman, J. W. VAST (Volume Annotation and Segmentation
878 Tool): Efficient Manual and Semi-Automatic Labeling of Large 3D Image Stacks. *Front Neural*
879 *Circuit* 12, 88 (2018).

880

881
882

883 **Methods**
884

885 *Animals*

886 All procedures were performed after evaluation by the Royal Netherlands Academy of Arts and
887 Sciences (KNAW) Animal Ethics Committee (DEC) and Central Authority for Scientific
888 Procedures on Animals (CCD, license AVD8010020172426). The specific experimental designs
889 were evaluated and monitored by the Animal Welfare Body (IvD, protocols NIN19.21.01,
890 NIN19.21.09 and NIN19.21.12). Male and female PV-Cre; Ai14, Rbp4-Cre or Rbp4-Cre; ChETA
891 mice were used in this study that were kept at a 12h day-night cycle with access to food *ad libitum*.
892 At 8 weeks of age, mice were fed either food with or without 0.2% cuprizone (biscyclohexane
893 oxaldihydrazone, Sigma-Aldrich) supplement (range: 5-6 weeks). During this time, the weight and
894 overall welfare of the mice was closely monitored.
895

896 *Plasmids*

897 Cre-dependent mt-GFP and mt-GCaMP6f AAV plasmids was created by replacing the mCherry
898 open reading frame (ORF) in pAAV-EF1a-mCherry-DIO (Addgene plasmid #20299, RRID:
899 Addgene_20299) with mt-GFP or 4mt-GCaMP6f ('mt-GcAMP6f' in the main text). High-Fidelity
900 Phusion Taq polymerase (Thermo Fisher Scientific, F-530XL) was used to amplify mt-GFP from
901 Addgene plasmid #44385 (RRID: Addgene_44385) or 4mt-GCaMP6f (plasmid was generously
902 donated by Diego de Stefani). For mt-GFP, PCR fragment and plasmid were digested with AscI
903 and NheI (New England Biolabs). Because 4mt-GCaMP6f contains an NheI digestion site, to
904 create the mt-GCaMP6f-DIO plasmid, pAAV-EF1a-mCherry-DIO was digested with NheI,
905 blunted using T4 DNA Polymerase (New England Biolabs), digested with AscI and then
906 dephosphorylated using Antarctic Phosphatase (New England Biolabs). The 4mt-GCamP6f PCR
907 product was phosphorylated using T4 Polynucleotide Kinase (New England Biolabs) and digested
908 using AscI. Plasmid and insert were then ligated overnight at 16 °C (T4 DNA ligase, New England
909 Biolabs). After transformation into chemically competent *E.coli* and subsequent plasmid
910 purification, insertion and double inverted orientation (DIO) were confirmed using restriction
911 enzyme analysis and DNA sequencing. The plasmids were deposited to Addgene (mt-GFP-DIO
912 #174112; 4mtGCaMP-DIO: #179529). To test Cre-dependent expression, HEK293-T cells (HEK
913 293T/17 cell line, CRL-11268 obtained from ATCC; RRID:CVCL_1926) were transfected with

914 pAAV-EF1a-mt-GFP-DIO or pAAV-EF1a-mt-GCaMP6f-DIO only or pAAV-EF1a-mt-GFP-DIO
915 and pCAG-Cre (Addgene #13775; RRID Addgene_13775) using polyethylenimine (PEI). Briefly,
916 plasmid DNA (500 ng) was diluted in saline and then mixed with PEI, allowed to incubate for 20-
917 25 minutes and then applied dropwise to HEK293-T cells in a 6-well plate. MitoGFP or mt-
918 GCaMP6f expression was assessed the next day using a fluorescence microscope, which was
919 absent in the cells lacking or expressing only pCAG-Cre, confirming Cre-dependence.
920
921 mt-GFP primers :
922 FW: 5' – AATAGCTAGCATCATGTCCGTCCTGACG – 3'
923 RV: 5' - TAATGGCGCGCC GGAAGTCTGGACATTTATTTG – 3'
924 4mt-GCaMP6f primers:
925 FW: 5' – ACT TCG CTG TCA TCA TTT G– 3'
926 RV: 5' - GCTAGCCCACCATGTCCGTC– 3'
927 Sequencing primers:
928 FW: 5' – GGATTGTAGCTGCTATTAGC – 3'
929 RV: 5' – GGCAAATAACTTCGTATAGGA – 3'
930
931 *AAV production*
932 HEK293-T cells of low passage (<25) were kept in Dulbecco′s Modified Eagle′s Medium
933 (DMEM, Thermo Fisher Scientific #31966-047) containing 10% fetal calf serum (FCS, Thermo
934 Fisher Scientific A4766801) and 5% penicillin-streptomycin (Pen-Strep, Thermo Fisher Scientific
935 #15140122) at 37 °C and 5% CO_2. For virus production, cells were plated on 15 cm dishes at a
936 density of 1-1.25 × 10^7 cells per dish (12 dishes per virus). The next day, medium was replaced
937 with Iscove's Modified Dulbecco's Medium (IMDM, Sigma Aldrich I-3390) containing 10% FCS,
938 5% Pen-Strep and 5% glutamine (Thermo Fisher Scientific #25030081) 1-2 hours before
939 transfection. For transfection, AAV rep/cap, AAV helper (mt-GFP: AAV5; mt-GCaMP6f: AAV1)
940 and transfer plasmids were mixed and diluted in saline before mixing with saline-diluted
941 polyethylenimine (PEI, Polysciences #23966-2) and brief vortexing. After 20-25 minutes of
942 incubation, the transfection mix was added in a drop-wise fashion to the culture plates. The next
943 day, all medium was refreshed after which the cells were left for an additional two nights (*i.e.* 72
944 hours after transfection). Medium was discarded and cells were then collected and subsequently

945 lysed with 3 freeze-thaw cycles to release AAVs. Cell lysate was then loaded on an iodixanol
946 gradient (60, 40, 25 and 15% iodixanol, ELITechGroup #1114542) in Beckman Quick-Seal
947 Polyallomer tubes (Beckman-Coulter #342414) which were sealed and centrifuged in a Beckman-
948 Coulter Optima XE-90 Ultracentrifuge at 16 °C and 69,000 rpm for 1 hour and 10 minutes. The
949 virus-containing fraction was extracted from the tubes and AAVs were then concentrated in
950 Dulbecco's Phosphate Buffered Saline (D-PBS) + 5% sucrose using Amicon Ultra-15 (100K) filter
951 units (Merck Millipore UFC910024) at 3220 *g*. At least 4 rounds of centrifugation were used to
952 ensure complete replacement of iodixanol with D-PBS + 5% sucrose. Typical yields were ~150 µl
953 of virus, the titer of which was determined using quantitative PCR (titers: mt-GFP-DIO, 4.43 ×
954 10^{13} gc/ml; mt-GCaMP6f-DIO, 3.44 × 10^{13} gc/ml)[83]. Viral aliquots were stored at −80 °C until
955 further use.
956
957 qPCR primers, recognize AAV2 Inverted Terminal Repeats (ITRs):
958 5' – GGAACCCCTAGTGATGGAGTT – 3'
959 5' – CGGCCTCAGTGAGCGA – 3'
960
961 *Viral injection*
962 Viral injections were typically performed during the 3rd week of control powder food or cuprizone
963 treatment. Mice were anaesthetized using isoflurane (3% induction, 1.2–1.5% maintenance) after
964 which they subcutaneously received 5mg/kg Metacam. Body temperature was monitored and
965 maintained at 37 °C using a heating pad and eyes were prevented from drying out using eye
966 ointment to prevent. The head was then shaved and placed in a stereotaxic frame (Kopf) and an
967 incision was made in the skin along the midline. Lidocaine (10%) was administered on the periost
968 before removing it. Small (<1 mm) bilateral craniotomies were made at -0.5 mm caudally from
969 Bregma and 2.5 mm laterally from the midline without damaging the dura mater. With a sharp
970 glass pipet attached to a Nanoject III (Drummond), 40-50 nL of virus was injected at 1 nL/second
971 and at a depth of 450 µm. Approximately 3 minutes after finishing the injection, the needle was
972 retracted slowly. Bone wax was applied to the craniotomies and the skin was sutured before the
973 animal was allowed to recover.

974

975 *Acute slice preparation*

976 After 5-6 weeks of cuprizone or control treatment (*i.e.* 2-3 weeks after virus injection), mice were
977 deeply anaesthetized using pentobarbital (50 mg/kg, intraperitoneal injection) and transcranially
978 perfused with ice-cold carbogenated (95% O_2, 5% CO_2) cutting artificial cerebrospinal fluid
979 (cACSF; 125 mM NaCl, 3 mM KCl, 6 mM $MgCl_2$, 1 mM $CaCl_2$, 25 mM glucose, 1.25 mM
980 NaH_2PO_4, 1 mM kynurenic acid and 25 mM $NaHCO_3$). After quickly dissecting out the brain 400
981 µm thick parasagittal slices were cut in ice-cold carbogenated cACSF using a Vibratome (1200S,
982 Leica Microsystems). Slices were transferred to a holding chamber containing carbogenated
983 cACSF where they were kept at 35 °C for 35 min to recover and then allowed to return to room
984 temperature for at least 30 min before starting experiments.

985

986 *Electrophysiology and two-photon imaging*

987 To perform electrophysiological experiments, slices were transferred to a recording chamber with
988 continuous in- and outflow of carbogenated recording ACSF (rACSF, 125 mM NaCl, 3 mM KCl,
989 1 mM $MgCl_2$, 2 mM $CaCl_2$, 10 mM glucose, 5 mM L-Lactate, 1.25 mM NaH_2PO_4, and 25 mM
990 $NaHCO_3$) at a rate of 1-2 ml per minute at 32 °C. Glass pipettes with an open tip resistance of 6-7
991 MΩ were filled with an intracellular solution containing (in mM, 130 K-Gluconate, 10 KCl, 10
992 HEPES, 4 Mg-ATP, 0.3 Na_2-GTP, 10 Na_2-phosphocreatine; pH ~7.25, osmolality ~280
993 mOsmol/kg) supplemented with 5 mg/ml biocytin (Sigma-Aldrich, B4261) and 50 µM Atto-594
994 (Sigma-Aldrich, A08637). Whole-cell recordings were made using a patch-clamp amplifier
995 (Multiclamp 700B, Axon Instruments, Molecular Devices, RRID: SCR_018455) operated by
996 AxoGraph X software (version 1.5.4; RRID: SCR_014284). Action potential trains were evoked
997 using 700 ms step pulses, from −250 pA to +700 nA with increments of 50 pA. Single action
998 potentials were evoked using 3 ms incremental (2.5-5 pA) step pulses with a starting amplitude
999 below spike threshold. Using an AD/DA converter (ITC-18, HEKA Elektronik GmbH), voltage
1000 was digitally sampled at 100 Hz. The access resistance during current-clamp experiments (range:
1001 15–30 MΩ) was fully compensated using bridge balance and capacitance neutralization of the
1002 amplifier. Somatic single-cell recordings were made from mt-GFP^+ cells, which were visualized
1003 using a two-photon (2P) laser-scanning microscope (Femto3D-RC, Femtonics Inc., Budapest,
1004 Hungary). Imaging was controlled using MES software (Femtonics Inc., Budapest, Hungary,

1005 version 6.3.7902). A Ti:Sapphire pulsed laser (Chameleon Ultra II, Coherent Inc., Santa Clara,
1006 CA, USA) was tuned to 770 nm for two-photon excitation to visualize mt-GFP/mt-GCaMP6f and
1007 tdTomato. Fluorescent signals were detected using two photomultipliers (PMTs, Hamamatsu
1008 Photonics Co., Hamamatsu, Japan), one for mt-GFP and for Atto-594 (20 μM) to assess its
1009 diffusion, as an indication of biocytin diffusion. For motility imaging, *z*-stacks were acquired every
1010 10 s for 8-12 mins. The Image Stabilizer plugin for FIJI was used to account for drift. For Ca^{2+}
1011 imaging, mt-GCaMP6f^{+} cells were targeted for single-cell patch clamping and filled with Atto-
1012 594 (50 μM) and biocytin (5 mg/ml). Next, *z*-stacks were made with the laser tuned to 800 nm to
1013 identify the axon using the Atto-594 signal. Axons were clearly distinguishable from dendrites, as
1014 they are much thinner, branch much more often and tend to project back towards the soma, as
1015 described previously[20]. Mitochondrial Ca^{2+} responses were then visualized with the laser tuned to
1016 940 nm and recorded at ~20 Hz imaging frequency. Ca^{2+} responses were analysed using a custom-
1017 written Matlab script. Briefly, regions of interest containing mitochondria were selected from
1018 which background was subtracted, bleach correction and smoothing were applied, and ΔF/F was
1019 calculated. Care was taken to keep the number of APs, which were evoked using a 700 ms block
1020 pulse, the same between groups (MBP^{-}, 105.6 ± 0.89 action potentials; MBP^{+}, 103.6 ± 0.51 APs;
1021 cuprizone, 104.7 ± 1.06 APs, Kruskal-Wallis test P = 0.1591). MBP^{-} segments do not include
1022 AISs.
1023

1024 *Immunohistochemistry*

1025 For staining of biocytin-filled cells, upon completion of experiments acute slices were immediately
1026 placed into 4% PFA in PBS for 20-25 minutes, followed by 3 washes of 10 minutes with PBS.
1027 Next, tissue was blocked for 2 hours in PBS containing 1-2% Triton-X and 10% normal goat
1028 serum. After blocking, sections were moved to blocking buffer containing primary antibodies (see
1029 **Supplementary Table 1**) and were incubated overnight at room temperature. Following three 10
1030 min washes in PBS, sections were transferred to PBS containing secondary antibodies and were
1031 incubated overnight two hours room temperature or overnight at 4 °C. The tissue was finally
1032 washed again in PBS three times for 10 minutes before mounting using FluorSave mounting
1033 medium (Merck-Millipore #345789). For immunostainings against MBP, the staining protocol
1034 was adjusted: blocking was done one hour at 37 °C and one hour room temperature and using 1%
1035 Triton, tissue was washed only once in PBS per washing step, and secondary antibodies were

1036 incubated one hour at 37 °C and one hour room temperature. For immunostainings on sections
1037 without biocytin-filled cells, 400 µm PFA-fixed sections were first cryoprotected by placing them
1038 into 30% sucrose-PBS solution until fully saturated. A sliding freezing microtome (Zeiss Hyrax
1039 S30; temperature controlled by a Slee Medical GmbH MTR fast cooling unit) was used to cut 40
1040 µm sections, which were either placed in PBS for immediate use or stored at −20 °C in
1041 cryoprotectant solution (30% ethylene glycol, 20% glycerol, 0.05 M phosphate buffer) until further
1042 use. Immunostaining protocol was the same as for 400 µm sections, but the blocking buffer
1043 contained 0.5% Triton-X and incubation duration for secondary antibodies was two hours at room
1044 temperature. All steps are performed with gentle shaking, with the exception of the 37 °C
1045 incubation steps. For analysis of normal and demyelinated subcortical white matter, Rbp4-Cre
1046 mice injected with AAV1-EF1a-mCherry-DIO and AAV5-EF1a-mtGFP-DIO (mixed 1:1) were
1047 first perfused with 1x PBS followed by 4% PFA-PBS. Brains were then dissected out and allowed
1048 to fix O/N in 4% PFA-PBS after the brains were cryoprotected using 30% sucrose-PBS and
1049 processed into 40 µm coronal sections as described above.
1050
1051 *Confocal microscopy*
1052 Imaging was performed using a Leica SP5 or SP8 X confocal laser scanning microscope controlled
1053 by Leica Application Suite AF. Biocytin-filled cells were imaged with a 63× oil-immersion lens
1054 using the tile-scan function with automated sequential acquisition of multiple channels enabled.
1055 Step sizes in the Z-axis were 0.3-0.75 µm, and images were collected at a 2048 × 2048 pixel
1056 resolution at 100-150 Hz. Mitochondria at AISs were imaged similarly, but only cells were imaged
1057 whose AIS was directed parallel to the imaging plane, and *z*-stack step sizes were 0.2 µm. Cellular
1058 reconstructions and quantification of mitochondrial density and morphology in single cells or at
1059 the AIS were performed manually using Neurolucida Software (MBF Bioscience, version
1060 2020.1.3, 64 bit, RRID: SCR_001775). In PV^+ interneurons, axons could easily be distinguished
1061 from dendrites based on their small diameter and extensive branching. Mitochondrial contours
1062 were drawn at the plane where the mt-GFP signal was brightest and was omitted when neurite
1063 branches deviated strongly from a parallel orientation with respect to the imaging plane (their
1064 location was still marked for density calculations). Mitochondria were counted as belonging to the
1065 reconstructed cell if the mt-GFP signal was located clearly inside the cytosol and followed the path
1066 of the reconstructed neurite. After completion of tracing, reconstructions and contours were

1067 analysed using Neurolucida Explorer (MBF Bioscience, 2019.2.1, RRID: SCR_017348), which
1068 calculated contour area, aspect ratio (length:width), density, axonal length and inter-mitochondrial
1069 distance. For analysis of mitochondrial densities at the myelin sheath, the MBP signal was turned
1070 off during tracing of PV^+ axons and marking their mitochondria, and *vice versa*. FIJI (RRID:
1071 SCR_002285) was used to extract partial images for use in figures. After preprocessing in FIJI,
1072 Imaris software (Oxford Instruments, version 9.7.2, RRID: SCR_007370) was used to generate
1073 three-dimensional surface renderings. The spot functionality of Imaris was used to count
1074 mitochondria in the field of view for motility analysis. Motile mitochondria were identified by eye,
1075 mitochondria were considered stable if they displaced less than 2 µm.
1076
1077 *3D Electron microscope data analysis*
1078 3D EM data was obtained from the Microns dataset[38] (www.microns-explorer.org). Basket
1079 interneurons were identified based on their morphology, *i.e.* their relatively round soma (as
1080 opposed to a pyramidal shape), the lack of spines on dendrites and a thin and highly branched axon
1081 that was partly myelinated. From each cell, one to two volumes were selected that either contained
1082 an axonal branch point with one myelinated and one unmyelinated branch, or a single branch with
1083 intermittent myelination. The EM volume of interest and cytosolic segmentation were then
1084 downloaded, after which the mitochondria were segmented and the segment length traced
1085 manually using Volume Annotation and Segmentation Tool (VAST) software (version 1.4.1)[84].
1086 Because we found that branch points in PV^+ interneurons are often nodes of Ranvier (a specialized
1087 axonal compartment), branch points and mitochondria that resided in them were not included in
1088 the analysis. Boutons were excluded for the same reason. If a mitochondrion spanned a border
1089 between myelinated and unmyelinated axon or beyond a branch point, they were not included. To
1090 analyse the mitochondrial content in L2/3 PNs, we used the same approached as described above.
1091 These cells were readily identified based on their pyramidal shape, spiny dendrites and distance
1092 from the pia. We selected L2/3 PNs that displayed patchy myelin. Fully or unmyelinated L2/3 PN
1093 axons were not included. Length and volume measurements were performed and exported using
1094 VAST Tools Matlab scripts. For examples used in figures, 3D models were exported as OBJ files
1095 using VAST software and rendered using 3ds Max (Autodesk, version 25.0.0.997, SCR_014251).
1096 See **Supplementary Table 2** for cells used in the analysis.
1097

1098 *Statistical analyses*

1099 All statistical comparisons were done using Prism (Graphpad, version 8.4.3, RRID: SCR_002798).
1100 Normality of datasets was determined using D'Agostino & Pearson or Shapiro-Wilk tests. We
1101 applied non-parametric tests if data deviated significantly from a normal distribution. For
1102 comparisons between groups we used a two-tailed unpaired t-test (normal data) or a two-tailed
1103 Mann-Whitney test (non-normal data). For t-tests degrees of freedom (df) are reported in the figure
1104 legends. One-way ANOVA (normal data) or Kruskal-Wallis test (non-normal data) was applied
1105 for comparisons of three groups; two-way ANOVA was used to test interactions between groups
1106 and treatments; Bonferroni's post hoc test (normal data) or Dunn's post hoc test (non-normal data)
1107 was used for multiple comparisons; nested t-tests or nested one-way ANOVAs were used when
1108 large numbers of datasets were involved (*i.e.* mitochondrial contours) to avoid overpowering of
1109 non-nested statistical tests (cells were nested inside their respective treatment groups). Figure
1110 legends contain *P*-values and *n*-numbers and whether the latter signify mice, cells or mitochondria.
1111 Means are presented with SEM.

1112

1113 **Data availability**

1114 All data and code are available upon request to the authors.

1115

1116 **Acknowledgments**

1117 The authors are thankful to Fred de Winter and Joost Verhaagen (NIN–KNAW) for the support
1118 for developing and producing the AAV constructs. We thank Christian Lohmann for critical
1119 reading of the manuscript and feedback during this research. We thank Diego de Stefani for
1120 generously sharing the 4mt-GCaMP6f plasmid with us. We thank Christiaan Levelt for
1121 generously sharing the AAV1-CAG-Flex-mRuby2-GSG-P2A-GCaMP6f virus with us. We thank
1122 Arnoldo Zaldivar Castro for optimizing the immunohistochemistry protocol.

1123

1124 **Funding**

1125 The Dutch Research Council NWO Vici 865.17.003 (MK)
1126 ZonMW Off Road 04510012010066 (KK)
1127 Erasmus scholarship G ATHINE 01 (MEB)

1128

Author contributions

Conceptualization: MK, KK

Methodology: MK, KK, MEB, BV

Investigation: KK, MEB, BV, NP

Formal analysis, MK, KK, MEB, BV

Visualization: MK, KK

Funding acquisition: MK

Project administration: MK

Supervision: MK, KK

Writing – original draft: KK

Writing – review & editing: MK, KK

Competing interests

Authors declare that they have no competing interests

1144 **Supplementary Figures**
1145
1146
1147

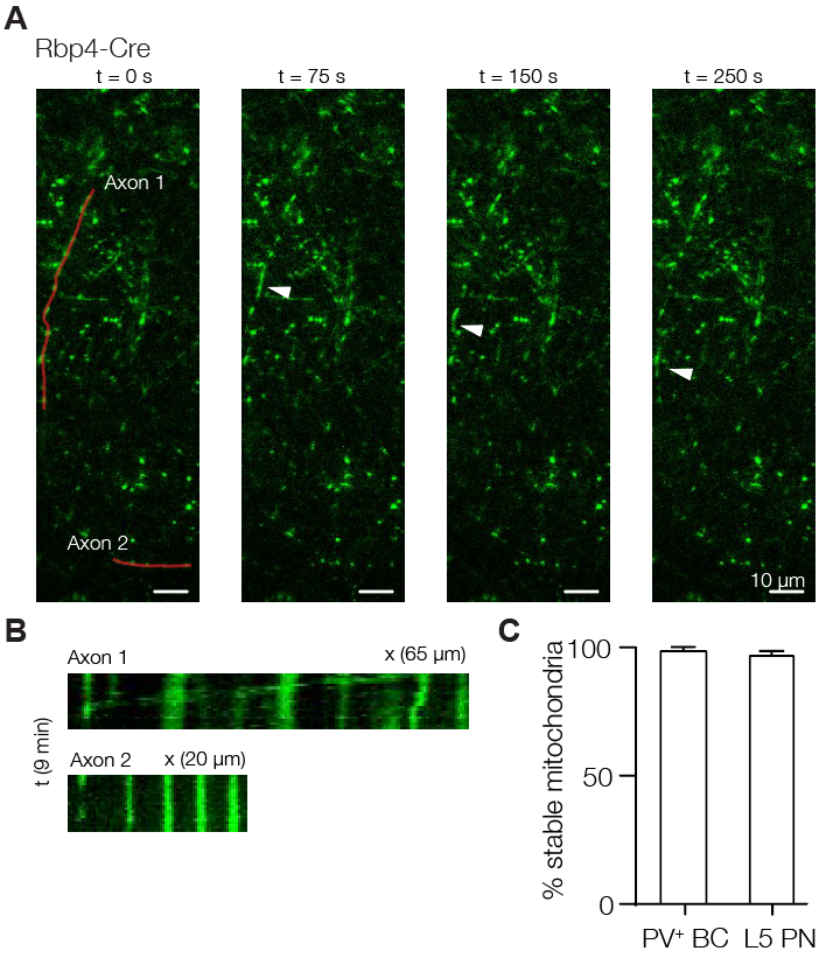

1148
1149 **Supplementary Figure 1 - Mitochondrial motility in acute brain slices (A)** Example frames
1150 showing motile mitochondria (mt-GFP, green) in one L5 PN axon, but all other mitochondria are
1151 stationary. Red lines indicate paths used for kymographs in b. **(B)** Example kymographs showing
1152 mitochondrial motility (1) and stability (2). **(C)** Quantification of stationary mitochondria in PV^+
1153 interneurons (PV^+ basket cells (BC); PV-Cre; Ai14 mice, n = 4) or L5 PNs (Rbp4-Cre mice, n =
1154 3). PV-Cre; Ai14, n = 11/1236; Rbp4-Cre, n = 23/1145 motile mitochondria/total mitochondria.
1155

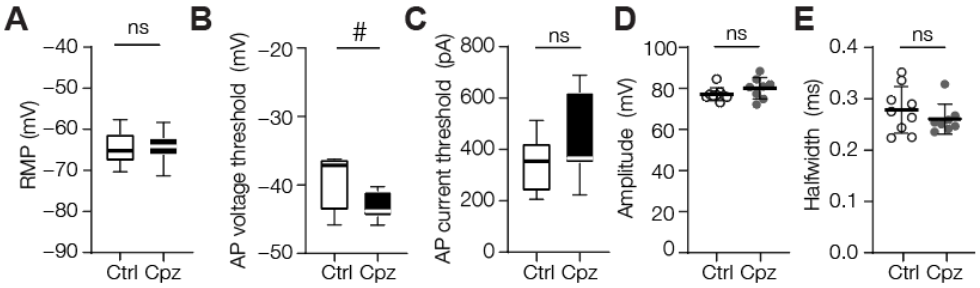

Supplementary Figure 2 – Action potential parameters and mitochondrial distribution at the AIS upon demyelination. (A) No change in resting membrane potential (RMP; unpaired t-test, $P = 0.7249$; control, $n = 9$ cells from 5 mice; cuprizone, $n = 8$ cells from 5 mice). **(B)** Voltage threshold shows a trend towards reduction upon cuprizone-mediated demyelination (unpaired t-test, $P = 0.0590$; control, $n = 9$ cells from 5 mice; cuprizone, $n = 8$ cells from 5 mice); No difference between control and cuprizone-treated groups in **(C)** current threshold (unpaired t-test, $P = 0.2066$), **(D)** AP amplitude (unpaired t-test, 0.1697) or **(E)** halfwidth (unpaired t-test, $P = 0.3489$; control, $n = 9$ cells from 5 mice; cuprizone, $n = 8$ cells from 5 mice). Horizontal bars indicate the mean, individual data points represent cells, error bars indicate SEM; Box plots represent the 25th to 75th percentiles, whiskers indicate the maximal and minimal values, solid line represents the median.

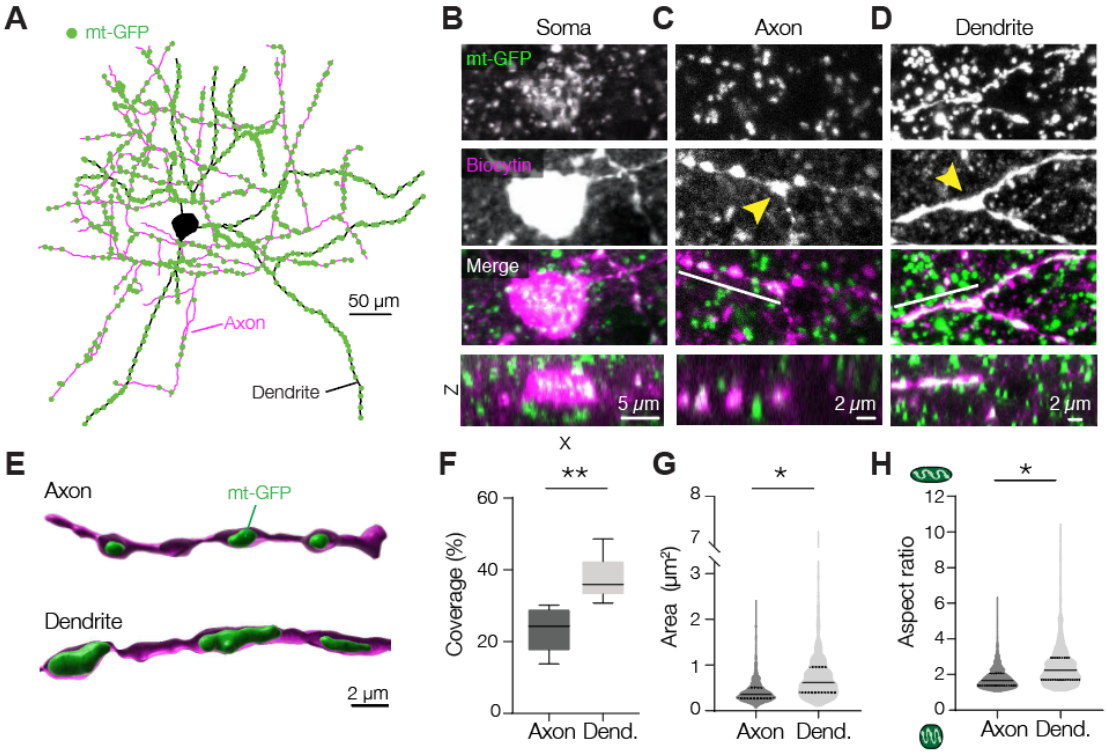

Supplementary Figure 3 – Axonal and dendritic PV⁺ interneuron mitochondria are morphologically distinct. (A) Example of a reconstructed PV⁺ interneuron and the locations of its mitochondria (green). Magenta, axon; black, dendrite. Mitochondria in soma were not quantified. **(B)** Examples of somatic, **(C)** axonal and **(D)** dendritic mitochondria in PV⁺ interneurons. Yellow arrowheads indicate branch points, white lines indicate axis used for *XZ* views. **(E)** 3D surface rendering of example axonal or dendritic mitochondria. **(F)** Percentage of PV⁺ neurite length covered by mitochondrial length (unpaired t-test, $^{**}P = 0.0093$; df = 8; Axon, n = 188 mitochondria; dendrite, n = 482 mitochondria; 5 cells from 3 mice). **(G)** Area of mitochondria is larger in PV⁺ dendrites (nested t-test, $^{*}P = 0.0144$; df = 8; Axon, n = 859 mitochondria; dendrite, n = 1138 mitochondria; 5 cells from 3 mice). **(H)** Aspect ratio of mitochondria is higher in PV⁺ dendrites, reflecting a more elongated morphology (nested t-test, $^{*}P = 0.0318$; df = 8; Axon, n = 859 mitochondria; dendrite, n = 1138 mitochondria; 5 cells from 3 mice). Box plots (f-h) represent the 25th to 75th percentiles, whiskers represent the maximal and minimal values, solid line represents the median. Solid lines in truncated violin plots represent the median, dotted lines represent 25th and 75th quartiles.

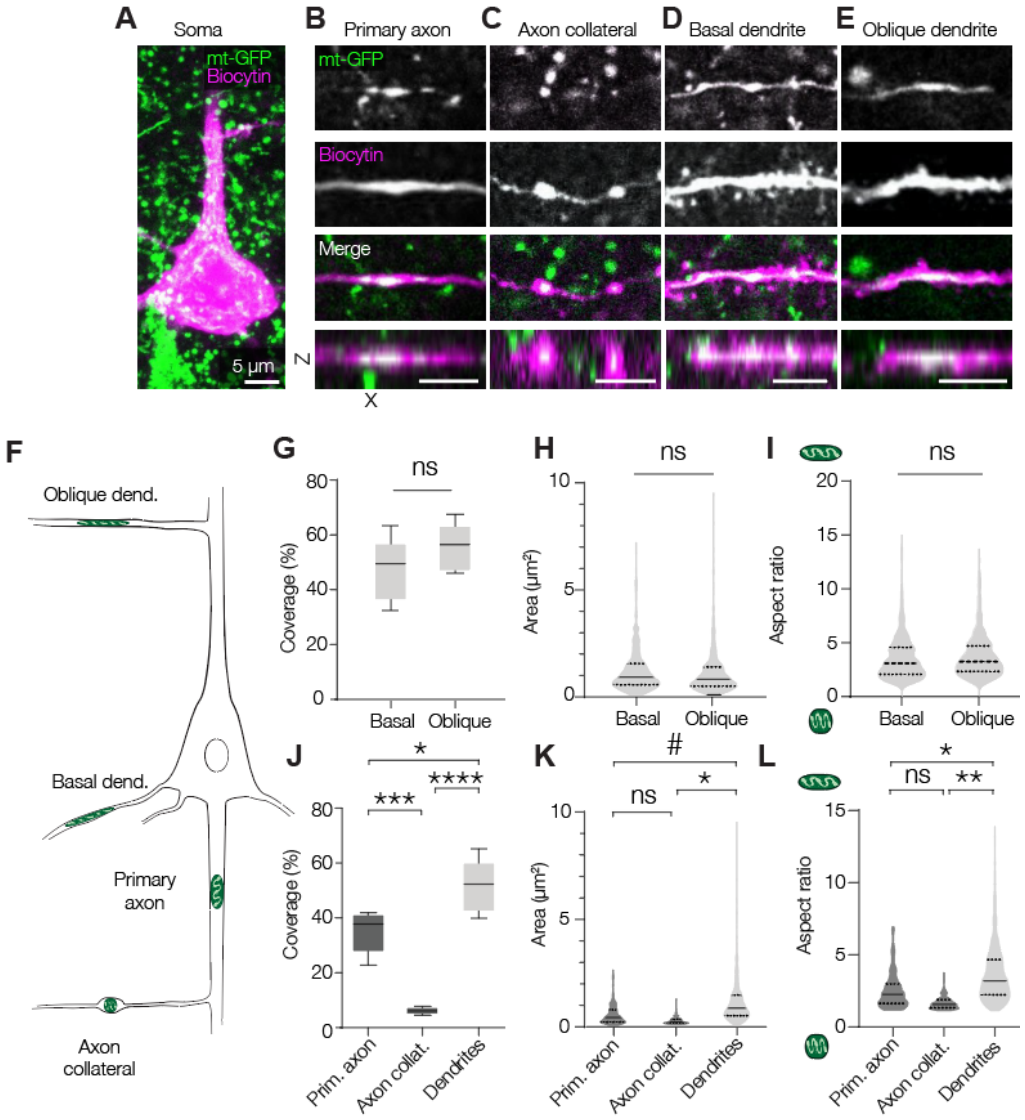

Supplementary Figure 4 – Axonal mitochondria are distinct from those in dendrites in L5 PNs. Example images of mitoGFP-labeled mitochondria in the **(A)** soma, **(B)** primary axon, **(C)** axon collateral, **(D)** oblique dendrite branch or **(E)** basal dendrite of a L5 PN. Somatic mitochondria were not quantified. **(F)** Schematic of subcellular compartments of the L5 PN that were investigated. **(G)** Dendritic coverage is not different between basal and oblique dendrites (unpaired t-test, $P = 0.2538$; basal dendrites, $n = 321$; oblique dendrites, $n = 331$ mitochondria from 5 cells of 3 mice each for each). **(H)** Mitochondria from basal and oblique dendrites have similar surface area (nested t-test, $P = 0.9554$) and **(I)** aspect ratio (nested t-test, $P = 0.7162$; basal dendrites, $n = 321$; oblique dendrites, $n = 331$ mitochondria from 5 cells of 3 mice each for each). **(J)** Neurite length covered by mitochondrial length (one-way ANOVA, $P < 0.0001$; Bonferroni's post hoc test, Primary axon vs axon collaterals, ***$P = 0.0001$; primary axon vs dendrites, **$P = 0.0141$; axon collateral vs dendrites, ****$P < 0.0001$; primary axon $n = 188$, axon collateral $n = 125$, dendrites $n = 652$ mitochondria; for each, $n = 5$ cells from 3 mice). **(K)** Mitochondrial area in L5 PNs is largest in dendrites and smallest in axon collaterals (nested one-way ANOVA, *$P = 0.0192$; Bonferroni's post hoc test, primary axon vs axon collaterals $P > 0.9999$; primary axon vs

1215 dendrites, #P = 0.0917; axon collaterals vs dendrites, *P = 0.0241; primary axon n = 188, axon
1216 collateral n = 125, dendrites n = 652 mitochondria; for each, n = 5 cells from 3 mice). **(L)**
1217 Mitochondria are significantly more round in L5 PN axons compared to dendrites (nested one-way
1218 ANOVA, P = 0.0031; Bonferroni's post hoc test, primary axon vs axon collaterals, P = 0.5094;
1219 primary axon vs dendrites, **P = 0.0418; axon collaterals vs dendrites, ***P = 0.0031; primary
1220 axon n = 188, axon collateral n = 125, dendrites n = 652 mitochondria; for each, n = 5 cells from
1221 3 mice). Box plots represent the 25th to 75th percentiles, whiskers represent the maximal and
1222 minimal values, solid line represents the median. In truncated violin plots, solid lines represent the
1223 median, dotted lines represent 25th and 75th quartiles.
1224

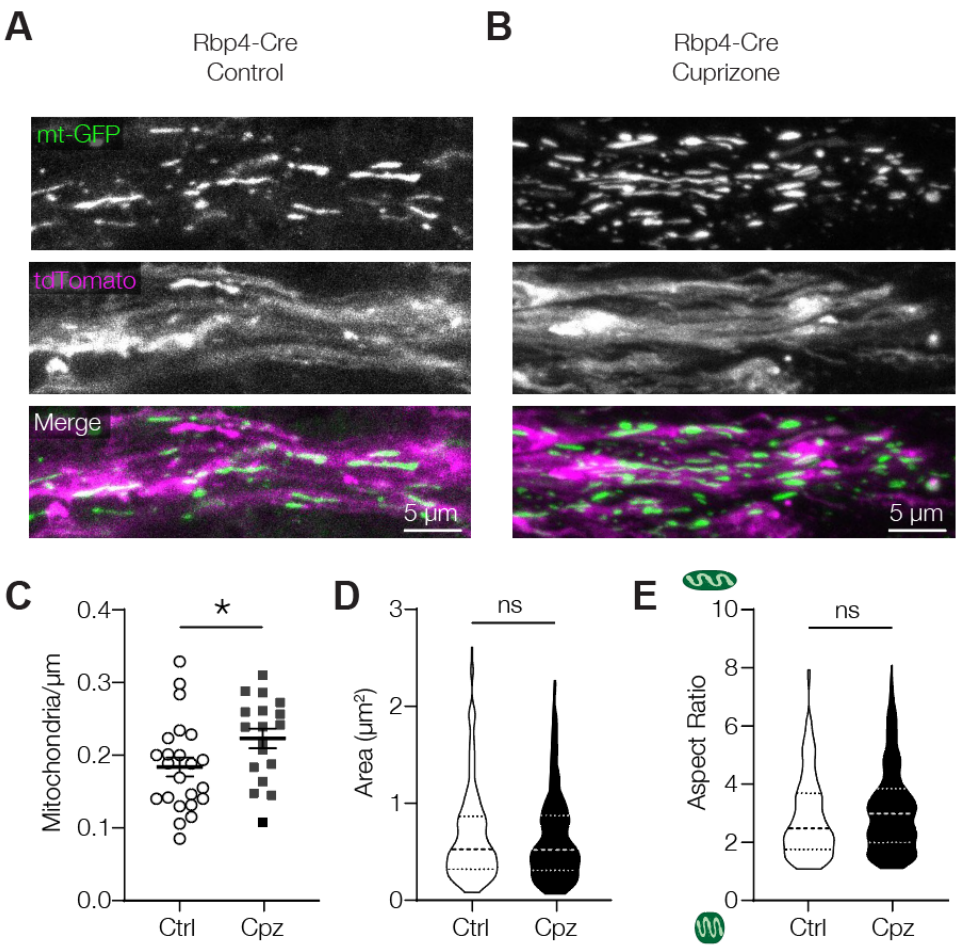

Supplementary Figure 5 – Increased mitochondrial density in the demyelinated white matter excitatory axons. (A-B) Example confocal images of mitochondria in the white matter of control (A) or cuprizone-treated (B) L5 pyramidal neuron axons from Rbp4-Cre mice. **(C)** Increased density after cuprizone-mediated demyelination (unpaired t-test, **P* = 0.0441; control, *n* = 23 axons from 3 mice; cuprizone, *n* = 19 axons from 3 mice). **(D)** Mitochondrial size is unchanged after demyelination (nested t-test, *P* = 0.6886; control, *n* = 172 mitochondria from 23 axons of 3 mice; cuprizone, *n* = 162 mitochondria from 19 axons of 3 mice). **(E)** Comparable aspect ratio of mitochondria in control or cuprizone-treated white matter axons (nested t-test, *P* = 0.1668; control, *n* = 172 mitochondria from 23 axons of 3 mice; cuprizone, *n* = 162 mitochondria from 19 axons of 3 mice). Horizontal lines in c the mean, error bars represent SEM, individual data points indicate axons. In truncated violin plots, solid lines represent the median, dotted lines represent 25th and 75th quartiles.

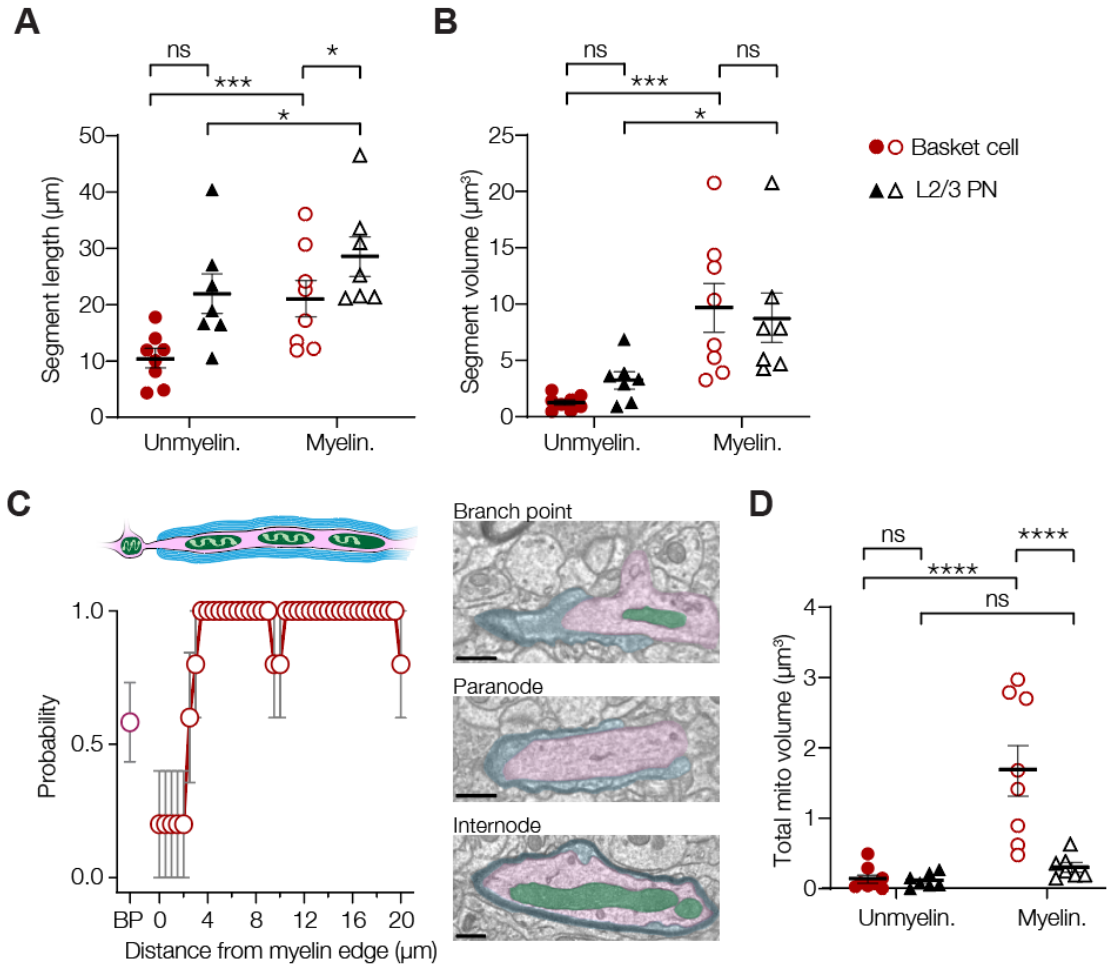

Supplementary Figure 6 – Myelination-dependent internode properties and mitochondria distribution

(A) Segment length of (un)myelinated axons in basket cells or L2/3 PNs (two-way ANOVA, myelination x cell type effect, $P = 0.2139$, $F_{(1,13)} = 1.708$; myelination effect, $P < 0.0001$, $F_{(1,13)} = 32.78$; cell type effect, $P = 0.0339$, $F_{(1,13)} = 5.619$; Bonferroni's post hoc test, basket myelinated vs. unmyelinated, ***$P = 0.0004$; PN myelinated vs. unmyelinated, *$P = 0.0195$; Myelinated basket vs PN, $P = 0.1804$; Unmyelinated basket vs PN *$P = 0.0253$). **(B)** Segment volume of (un)myelinated axons in basket cells or L2/3 PNs (two-way ANOVA, myelination x cell type effect, $P = 0.2765$, $F_{(1,13)} = 1.209$; myelination effect, $P = 0.0001$, $F_{(1,13)} = 28.30$; cell type effect, $P = 0.7825$, $F_{(1,13)} = 0.07945$; Bonferroni's post hoc test, basket myelinated vs. unmyelinated, ***$P = 0.0008$; PN myelinated vs. unmyelinated, *$P = 0.0265$; Myelinated basket vs PN, $P > 0.9999$; Unmyelinated basket vs PN $P = 0.7632$). **(C)** Probability of mitochondria occupancy at branch points (BP; presumed nodes) and along the myelinated internode. *Left:* Mitochondria are often found at branch points (probability 0.58; 12 branch points from 8 cells), show limited occupancy in the first ~2 µm of the internode and are distributed evenly and with high probability along the internode (5 internodes from 4 cells). *Right:* example EM images of a branchpoint containing a mitochondrion, a paranode devoid of mitochondria and an internode containing a large mitochondrion. Axons, myelin and mitochondria are pseudocoloured (magenta, blue and green, respectively). Scale bar, 500 nm. **(D)** Total volume of mitochondria in (un)myelinated axons

in basket cells or L2/3 PNs (two-way ANOVA, myelination x cell type effect, $P = 0.0027$, $F_{(1,13)} = 13.58$; myelination effect, $P = 0.0004$, $F_{(1,13)} = 22.16$; cell type effect, $P = 0.0052$, $F_{(1,13)} = 11.24$; Bonferroni's post hoc test, basket myelinated vs. unmyelinated, ****$P < 0.0001$; PN myelinated vs. unmyelinated, $P = 0.9925$; Myelinated basket vs PN, ****$P < 0.0001$; Unmyelinated basket vs PN $P > 0.9999$).

1267

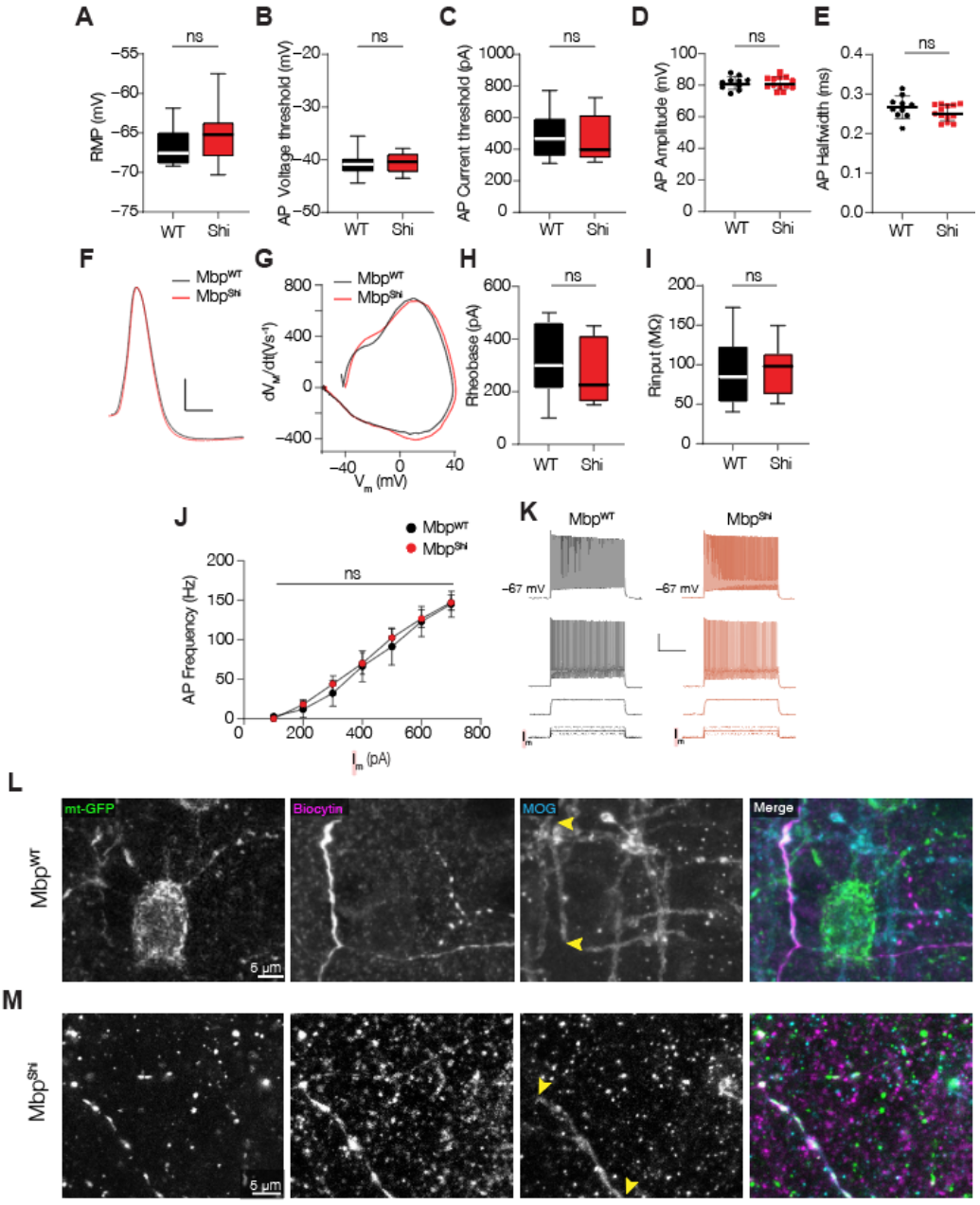

1268

1269 **Supplementary Figure 7 – Electrophysiological properties of PV⁺ interneurons in *Mbp^WT* or**
1270 ***Mbp^Shi* mice. (A)** Resting membrane potential (unpaired t-test, $P = 0.2597$; df = 18; *Mbp^WT*, $n = 8$
1271 cells from 3 mice; *Mbp^Shi*, $n = 12$ cells from 3 mice); **(B)** Action potential membrane threshold
1272 (unpaired t-test, $P = 0.8364$; df = 21; *Mbp^WT*, $n = 10$ cells from 3 mice; *Mbp^Shi*, $n = 13$ cells from
1273 3 mice); **(C)** Action potential current threshold (unpaired t-test, $P = 0.6566$; df = 21; *Mbp^WT*, $n =$
1274 10 cells from 3 mice; *Mbp^Shi*, $n = 13$ cells from 3 mice); **(D)** Action potential amplitude (unpaired
1275 t-test, $P = 0.9358$; df = 21; *Mbp^WT*, $n = 10$ cells from 3 mice; *Mbp^Shi*, $n = 13$ cells from 3 mice);
1276 **(E)** Action potential halfwidth (unpaired t-test, $P = 0.1744$; df = 21; *Mbp^WT*, $n = 10$ cells from 3
1277 mice; *Mbp^Shi*, $n = 13$ cells from 3 mice); **(F)** Example single action potential from either genotype,
1278 scalebar indicates 10 mV and 0.25 ms; **(G)** Phase-plane plots of the example traces in h; **(H)**

Rheobase (unpaired t-test, $P = 0.4395$; df = 18; Mbp^{WT}, $n = 8$ cells from 3 mice; Mbp^{Shi}, $n = 12$ cells from 3 mice); **(I)** Input resistance (unpaired t-test, $P = 0.8375$; df = 18; Mbp^{WT}, $n = 8$ cells from 3 mice; Mbp^{Shi}, $n = 12$ cells from 3 mice); **(J)** Comparable action potential firing frequency in Mbp^{WT} or Mbp^{Shi} mice (two-way ANOVA, $P = 0.9967$, $F_{(13, 221)} = 0.2488$; genotype effect $P = 0.7752$, $F_{(1, 17)} = 0.08422$; Mbp^{WT}, $n = 8$ cells from 3 mice; Mbp^{Shi}, $n = 12$ cells from 3 mice); **(K)** Example traces in response to 200, 400 or 600 pA somatic current injection, scale bar indicates 25 mV and 250 ms.). **(L-M)** Confocal images corresponding to the 3D renders in Figure 6. Yellow arrowheads indicate internodes. Individual data points in a-k represent cells, error bars indicate SEM; Box plots represent the 25th to 75th percentiles, whiskers indicate the maximal and minimal values, solid line represents the median.

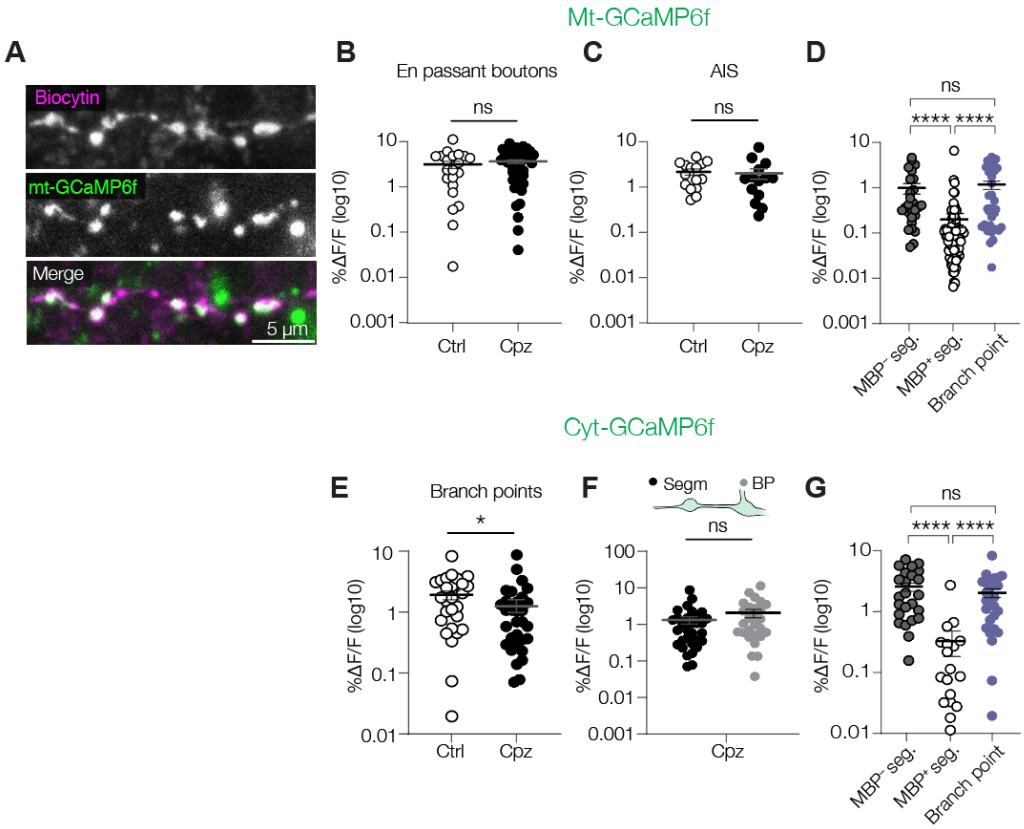

Supplementary Figure 8 – mt-Ca^{2+} and cyt-Ca^{2+} responses in PV^+ axons

(A) Example confocal image of PV^+ *en passant* boutons. **(B)** Demyelination does not alter mt-Ca^{2+} buffering in *en passant* boutons (Mann-Whitney test, $P = 0.2847$; control, $n = 21$ mitochondria of 4 cells from 2 mice; cuprizone, $n = 47$ mitochondria of 8 cells from 4 mice). **(C)** mt-Ca^{2+} responses at the AIS are not changed after demyelination (Mann-Whitney test, $P = 0.1694$; control, $n = 15$ mitochondria of 5 AISs from 3 mice; cuprizone, $n = 20$ mitochondria of 6 AISs from 4 mice). **(D)** In control PV^+ axons, amplitude of mt-Ca^{2+} responses at MBP^- segments are not different from those at branch points (Kruskal-Wallis test, $P < 0.0001$; Dunn's post hoc test, MBP^+ vs MBP^- $P = 0.0020$, MBP^- vs. branch points $P > 0.9999$; MBP^+ vs branch points $P < 0.0001$; MBP^+ segments, $n = 101$ mitochondria of 12 cells from 7 mice, same data as in Figure 7D; MBP^- segments, $n = 27$ mitochondria of 9 cells from 5 mice, same data as in Figure 7D; branch points, $n = 38$ mitochondria of 11 cells from 7 mice, same data as in Figure 8D); **(E)** Smaller cyt-Ca^{2+} transients in branch points after demyelination (Mann-Whitney test, $P = 0.0307$; control, $n = 27$ branch points of 7 cells from 3 mice; cuprizone, $n = 31$ branch points of 6 cells from 3 mice); **(F)** Cytosolic Ca^{2+} responses are comparable in segments and branch points upon demyelination (Mann-Whitney test, $P = 0.2476$; $n = 28$ segments of 6 cells from 3 mice, $n = 31$ branch points of 6 cells from 3 mice, same data as in E); **(G)** In control PV^+ axons, amplitude of cytosolic Ca^{2+} responses at MBP^- segments are not different from those at branch points (Kruskal-Wallis test, $P < 0.0001$; Dunn's post hoc test, MBP^+ vs MBP^- $P < 0.0001$, MBP^- vs. branch points $P > 0.9999$; MBP^+ vs branch points $P < 0.0001$; MBP^+, $n = 18$ segments of 6 cells from 3 mice; MBP^-, $n = 24$ segments of 8 cells from 3 mice, same data as in Figure 7F; branch points, control, $n = 27$ branch points of 7 cells from 3 mice, same data as in E).

1315
1316 **Supplementary Table 1**

1317

Antibody	Host	Dilution	Manufacturer	Catalog number	RRID
Anti-Green fluorescent protein	Chicken	1:500	Abcam	ab13970	AB_300798
Anti-Red fluorescent protein	Mouse	1:500	Abcam	ab65856 (discontinued)	AB_1141717
Anti-βIV Spectrin	Rabbit	1:1000	Engelhardt and Kole lab	N/A	N/A
Anti-Myelin Basic Protein	Mouse	1:250	Covance	SMI-99P	AB_10120129
Anti-Myelin Oligodendrocyte Glycoprotein	Mouse	1:250	Millipore	MAB5680	RRID:AB_1587278
Anti-Mouse-Alexa-405	Goat	1:500	ThermoFisher	A31553	AB_221604
Anti-Chicken-Alexa-488	Goat	1:500	ThermoFisher	A11039	AB_142924
Anti-Rabbit-Alexa-633	Goat	1:500	ThermoFisher	A21070	AB_2535731
Anti-Mouse-Alexa-647	Goat	1:500	ThermoFisher	A21235	AB_2535804
Streptavidin-Alexa-594	N/A	1:500	ThermoFisher	S11227	N/A
Streptavidin-Alexa-633	N/A	1:500	ThermoFisher	S32364	AB_2313500

1318

1319 Overview of antibodies and dilutions used in this study.

1320

1321 **Supplementary Table 2**

1322

Cell name	Neuroglancer ID	Cell type	Location of interest
PV1_1	864691135307240262	Basket cell	174508, 124118, 21157
PV1_2	864691135307240262	Basket cell	180056, 128599, 21514
PV2_1	864691135367308281	Basket cell	178363, 187957, 20579
PV3_1	864691135386593409	Basket cell	181574, 159259, 20999
PV3_2	**864691135386593409**	**Basket cell**	**191862, 145103, 20142**
PV4_1	864691135544579880	Basket cell	171765, 173397, 20706
PV5_1	864691135428608048	Basket cell	181752, 143942, 22968
PV6_1	864691135590150923	Basket cell	170564, 132985, 19749
PV7_1	864691135697462549	Basket cell	173603, 134391, 22067
PV8_1	864691136952074207	Basket cell	186366, 118464, 20183
PN_1	864691135855890478	L2/3 PN	144874, 149452, 23959
PN_2	864691135975539779	L2/3 PN	337852, 147425, 19387
PN_3	864691135564739159	L2/3 PN	334986, 157943, 20515
PN_4	864691136031786427	L2/3 PN	123284, 152471, 23565
PN_5	864691136618414989	L2/3 PN	222968, 137995, 23424
PN_6	864691135012580342	L2/3 PN	238983, 137249, 23366
PN_7	**864691135099882016**	**L2/3 PN**	**241318, 147339, 23370**

1323

1324 Overview of the cells used in the 3D EM analysis. Bold marked cells were used as examples in **Figure 5**.

1325
1326
1327
1328
1329
1330
1331
1332
1333
1334
1335
1336

1337
1338 **Supplementary Videos**
1339
1340

1341 **Supplementary Video 1**

1342 Heatmap of mitochondrial Ca^{2+} responses in a PV^{+} axons upon 100 APs. A significant response
1343 can be seen in the branch point but not under the myelin sheath. Video corresponds to Figure 7b.
1344
1345 **Supplementary Video 1**

1346 Heatmap of cytosolic Ca^{2+} responses in a PV^{+} axons upon 100 APs. In the AIS and the first branch
1347 point, significant responses are seen but not under the myelinated internode. Video corresponds to
1348 Figure 7e.
1349
1350